Monthly Notices
of the
ROYAL ASTRONOMICAL SOCIETY

Mon. Not. R. Astron. Soc. **423,** 505–528 (2012) doi:10.1111/j.1365-2966.2012.20895.x

Global models of runaway accretion in white dwarf debris discs

Brian D. Metzger,[1⋆]† Roman R. Rafikov[1⋆]‡ and Konstantin V. Bochkarev[1,2⋆]

[1]*Department of Astrophysical Sciences, Princeton University, Peyton Hall, Princeton, NJ 08544, USA*
[2]*Department of General and Applied Physics, Moscow Institute of Physics and Technology, Dolgoprudny 141700, Russia*

Accepted 2012 March 9. Received 2012 March 1; in original form 2012 February 2

ABSTRACT

A growing number of young white dwarfs (WDs) with metal-enriched atmospheres are accompanied by excess infrared (IR) emission, indicating that they are encircled by a compact dusty disc of solid debris. Such 'WD debris discs' are thought to originate from the tidal disruption of asteroids or other minor bodies. However, the precise mechanism responsible for transporting matter from the disruption radius to the WD surface remains unclear, especially in systems with the highest inferred metal accretion rates $\dot{M}_Z \sim 10^8$–$10^{10}\,\mathrm{g\,s^{-1}}$, which cannot be explained by Poynting–Robertson (PR) drag alone. Here we present global time-dependent calculations of the coupled evolution of the gaseous and solid components of WD debris discs. Solids transported inwards (initially due to PR drag) sublimate at tens of WD radii, producing a source of gas that both accretes on to the WD surface and viscously spreads outwards in radius, where it overlaps with the solid disc. Our calculations show that if the aerodynamic coupling between the solids and gaseous discs is sufficiently strong (and/or the gas viscosity sufficiently weak), then gas builds up near the sublimation radius faster than it can viscously spread away. Since the rate of drag-induced solid accretion increases with gas density, this results in a runaway accretion process, as predicted by Rafikov, during which the WD accretion rate reaches values orders of magnitude higher than can be achieved by PR drag alone, consistent with the highest measured values of $\dot{M}_Z$. We explore the evolution of WD debris discs across a wide range of physical conditions and describe the stages of the runaway process in detail. We also calculate the predicted distribution of observed accretion rates $\dot{M}_Z$, finding reasonable agreement with the current sample. We use our disc evolution model to show that the steady-state assumption commonly adopted to calculate WD metal accretion rates is inaccurate when the metal settling time in the WD atmosphere is long compared to the viscous time-scale; a long metal settling phase following a runaway accretion event may explain some metal-polluted WDs with no current IR excess. Although the conditions necessary for runaway accretion are at best marginally satisfied given the minimal level of aerodynamic drag between circular gaseous and solid discs, the presence of other stronger forms of solid–gas coupling – such as would result if the gaseous disc is only mildly eccentric – substantially increase the likelihood of runaway accretion.

Key words: accretion, accretion discs – protoplanetary discs – white dwarfs.

1 INTRODUCTION

A significant fraction, ∼10 per cent, of white dwarfs (WDs) with metal-enriched atmospheres (DAZ and DBZ types) and cooling ages $\lesssim$0.5 Gyr are accompanied by excess infrared (IR) emission (Zuckerman & Becklin 1987; Graham et al. 1990; Kilic et al. 2005; Kilic & Redfield 2007; von Hippel et al. 2007; Farihi, Jura & Zuckerman 2009; Debes et al. 2011a,b). This emission is well modelled as WD radiation reprocessed by an optically thick, geometrically thin disc of refractory material (Jura 2003; Jura, Farihi & Zuckerman 2007a). Modelling of the IR spectral energy distribution (SED) shows that the inner edge of the disc resides at $R_{\rm in} \sim$ several tens of WD radii $R_\star$, close to where the equilibrium temperature $T \sim 1500\,\mathrm{K}$ is sufficiently high to sublimate silicate dust grains. The outer edge of the disc is also well constrained by the SED at longer wavelengths, with its radius $R_{\rm out} \lesssim \mathrm{R}_\odot \approx 100R_\star$ typically found to exceed $R_{\rm in}$ by a factor of several (e.g. Jura et al. 2007b, 2009a; Debes et al. 2011b).

⋆E-mail: bmetzger@astro.princeton.edu (BDM); rrr@astro.princeton.edu (RRR); kbochkar@astro.princeton.edu (KVB)
†NASA Einstein fellow.
‡Sloan fellow.

No evidence is found for disc flaring from the SEDs of most systems (cf. Jura et al. 2007a), consistent with the disc material being concentrated in a thin, optically thick layer similar to the rings of Saturn (Cuzzi et al. 2010) (although there are a few examples of discs, including GD 56 and GD 362, where warps or flaring are needed to fit their SEDs; Jura et al. 2007a,b). Low-resolution spectroscopy with the Infrared Spectrograph on the *Spitzer Space Telescope* reveals an emission feature at 10 μm, indicating the presence of small, micron-sized silicate dust particles (Jura, Farihi & Zuckerman 2009b). Though small dust is clearly present in some discs, the detailed distribution of particle sizes is not well constrained. In this work we assume that most of the solid mass in the disc is concentrated in macroscopic particles with characteristic size $\sim$ cm, as is consistent with observations (Graham et al. 1990) and with theoretical estimates of the disc lifetime (see equation 59).

Several WDs with dusty discs also possess *gaseous* discs (Melis et al. 2010), as inferred by the detection of double-peaked emission lines of Ca II and Fe II (Gänsicke et al. 2006, 2008; Gänsicke, Marsh & Southworth 2007). These features clearly indicate a Keplerian disc composed primarily of gaseous, high-Z elements (no H emission lines have yet been detected) which is radially coincident with the dusty disc (Melis et al. 2010). Although most DZ WDs display no detectable emission lines, gaseous discs could in principle be more common because the disc line emission is easily overwhelmed by continuum emission from the WD photosphere.

Jura (2003) proposed that compact discs of metals around WDs are produced by the tidal disruption of asteroids or other minor bodies. A plausible source of such rocky bodies are objects placed on to low periastron orbits by gravitational perturbations from giant planets which have survived the asymptotic giant branch (AGB) phase of the WD progenitor (Duncan & Lissauer 1998; Debes & Sigurdsson 2002). Discs formed this way are often termed 'debris discs' since they result from the destruction of larger bodies, despite the fact that many of their properties (e.g. typical distance from the star and optical depth) are very different from conventional debris discs around young main-sequence stars (Wyatt 2008) as well as the much larger (tens of au) debris discs around very young, hot ($T \gtrsim 10^5$ K) WDs (Chu et al. 2011). A tidal disruption origin naturally explains why the outer radii of observed discs $R_{\rm out} \lesssim 1\ {\rm R}_\odot$ are similar to the Roche radius $R_{\rm R} \sim (M_\star/\rho_{\rm d})^{1/3} \sim {\rm R}_\odot$ of a self-gravitating object of typical density $\rho_{\rm d} \sim$ a few g cm^{-3}, where $M_\star \approx 0.6\,{\rm M}_\odot$ is the WD mass.

Asteroid-fed discs are also a promising explanation for the metals in the atmospheres of DZ WDs (Jura 2003), which otherwise are rapidly depleted by gravitational settling on a time-scale much shorter than the WD age (e.g. Paquette et al. 1986). One can estimate the (appropriately time-averaged) metal accretion rate $\dot{M}_Z$ in individual WD systems by combining the observed photospheric metal abundances with theoretical estimates of the mass in the outer convective zone of the WD and the settling times of heavy elements (e.g. Koester & Wilken 2006; Koester 2009). Values estimated in this way fall within the relatively wide range $\dot{M}_Z \sim 10^6$–10^{11} g s^{-1} (Farihi et al. 2009, 2010a).

Several additional lines of evidence now support the asteroid disruption model for WD debris discs and metal pollution. First, both gaseous and dusty discs are found exclusively around metal-rich WDs: from the statistics of systems observed with *Spitzer*, Farihi et al. (2009) estimate that $\sim$20 per cent of DAZ WDs host compact debris discs, yet no evidence is found for discs around WDs without metal pollution (e.g. Hansen, Kulkarni & Wiktorowicz 2006; Mullally et al. 2007). Farihi et al. (2010a) also found a strong positive correlation between the presence of a compact debris disc and the metal accretion rate $\dot{M}_Z$. The mass in the outer convective zone of many WDs is similar to that of an asteroid of several hundred km size, similar to Ceres or Vesta, while the relative abundances of several elements heavier than He are indeed similar to those in Solar system bodies formed interior to the ice line, such as the Earth, Moon and asteroids (Jura 2006; Zuckerman et al. 2007, 2010; Klein et al. 2010). Finally, the chief alternative theory for WD metal pollution, accretion from the interstellar medium, is now challenged by a variety of observations (e.g. Koester & Wilken 2006; Kilic & Redfield 2007; Jura et al. 2009a; Farihi et al. 2010a).

Despite growing evidence in support of the asteroid tidal disruption model, it remains unclear precisely what mechanisms are responsible for transporting metals from the disrupted ring of solids (with characteristic radius of several tens of $R_\star$) to the WD surface at the observed rates. The goal of this paper is to address this question with fully self-consistent global numerical models of the coupled evolution of the solid and gaseous components of WD debris discs.

1.1 Summary of previous work

We begin by summarizing previous theoretical work on accretion in WD debris discs. As mentioned above, the inner edge of the solid disc $R_{\rm in}$ is located near the sublimation radius $R_{\rm s}$ (Rafikov 2011a):

$$R_{\rm in} \simeq R_{\rm s} \equiv \frac{R_\star}{2}\left(\frac{T_\star}{T_{\rm s}}\right)^2 \approx 0.2\,{\rm R}_\odot \left(\frac{R_\star}{0.01\,{\rm R}_\odot}\right)\left(\frac{T_\star}{10^4\,{\rm K}}\right)^2\left(\frac{T_{\rm s}}{1500\,{\rm K}}\right)^{-2}, \quad (1)$$

where $T_{\rm s}$ is the sublimation temperature of silicate grains (we assume here that particle's emissivities for starlight and for its own thermal radiation are the same). Adopting a typical value for the WD radius $R_\star \approx 0.01\,{\rm R}_\odot$ (Ehrenreich et al. 2011) one finds $R_{\rm s} \approx 0.2\ {\rm R}_\odot$, consistent with observations (Jura et al. 2007b, 2009b).

It is worth noting that fitting the SEDs in some WD systems requires an unphysically high sublimation temperature $T_{\rm s}$ (e.g. Jura et al. 2007a; Brinkworth et al. 2009; Dufour et al. 2010; Melis et al. 2010). This suggests that other physics, such as a high particle albedo or conduction in the gas phase (Jura et al. 2007b), may play an important role, thereby calling the validity of equation (1) into question. These complications do not, however, affect the conclusions of this work since hereafter we scale all relevant distances to $R_{\rm in}$ without specifying what physics sets its value.

The sublimation of solid particles produces a source of metallic gas at $r \approx R_{\rm s}$. Viscosity redistributes gas from this location, producing an extended disc that transports mass from $R_{\rm s}$ to the stellar surface $R_\star$. If one assumes that the disc is turbulent, with an effective viscosity characterized by the conventional α-parametrization $\nu = \alpha c_{\rm s}^2/\Omega_{\rm K}$ (Shakura & Sunyaev 1973), then the viscous time at the sublimation radius is given by

$$t_\nu \sim \frac{R_{\rm s}^2}{\nu} \approx 2\times 10^3\,{\rm yr}\left(\frac{\alpha}{10^{-3}}\frac{T_{\rm g}}{5000\,{\rm K}}\right)^{-1}\left(\frac{\mu}{28 m_{\rm p}}\right) \times \left(\frac{M_\star}{0.6\,{\rm M}_\odot}\frac{R_{\rm s}}{0.2\,{\rm R}_\odot}\right)^{1/2}, \quad (2)$$

where $c_{\rm s} = (kT_{\rm g}/\mu)^{1/2}$ is the gas sound speed; $T_{\rm g}$ is the gas temperature, normalized to a value characteristic of the range $\approx$(3–7) $\times$ 10^3 K set by the balance between photoionization heating and metal line cooling (Melis et al. 2010); μ is mean molecular weight, normalized to a value $28 m_{\rm p}$ characteristic of pure Si; $\Omega_{\rm K} = (GM_\star/r^3)^{1/2}$

is the Keplerian angular velocity; and α is normalized to a value 10^{-3} somewhat lower than that expected to result from magnetohydrodynamical (MHD) turbulence in fully ionized discs (e.g. Davis, Stone & Pessah 2010), an assumption we discuss further in Section 6.

Equation (2) shows that the viscous time-scale is relatively short compared to other time-scales of relevance, such as the total disc lifetime, which is typically estimated to be $\lesssim 10^{4.5}$–$10^{6.5}$ yr (Girven et al. 2012). In most cases the accretion rate on to the stellar surface $\dot{M}_Z$ is thus ultimately controlled by the rate at which solids reach R_s, not by the maximum rate of gas accretion set by viscosity. A key theoretical question is thus how solids are transported to the sublimation radius at rates consistent with the range of values $\dot{M}_Z \sim 10^6$–$10^{10}\,\mathrm{g\,s^{-1}}$ inferred from observations.

One mechanism of solid disc evolution is angular momentum transport due to the interaction between disc particles (e.g. physical collisions), in full analogy with the rings of Saturn. However, as we show in Appendix A (see also Farihi, Zuckerman & Becklin 2008), for realistic assumptions about the size distribution and mass of the debris disc, the time-scale of this process is generally too long, resulting in a negligible accretion rate $\dot{M}_Z$.

Another more promising mechanism to drive solids inwards is Poynting–Robertson (PR) drag. Rafikov (2011a, hereafter R11a) demonstrated that PR drag produces accretion rates up to $\dot{M}_Z \sim \dot{M}_{\rm PR,in} \lesssim 0.03 L_\star/c^2 \sim 10^8\,\mathrm{g\,s^{-1}}$, where $\dot{M}_{\rm PR,in}$ is the maximum PR accretion rate for an optically thick disc of solids (as defined by equation 43 below) and $L_\star$ is the WD luminosity (see equation 22). Bochkarev & Rafikov (2011, hereafter BR11) followed this work by computing *global* models of the disc evolution under the action of the PR drag. By considering a variety of initial conditions, including both optically thin and optically thick debris discs, they showed that the results of R11a hold quite generally.

Fig. 1 shows the measured distribution of WD metal accretion rates $\dot{M}_Z$ from the samples of Farihi et al. (2009, 2010b). We normalize $\dot{M}_Z$ to $\dot{M}_{\rm PR,in}$ calculated using equation (22), to be introduced later in Section 3, assuming $R_{\rm in} \simeq R_s$ (equation 1) and using the measured effective temperature of each WD in the sample. Fig. 1 shows that a significant fraction of those WD systems with an IR excess (indicative of ongoing metal accretion) have $\dot{M}_Z \sim \dot{M}_{\rm PR,in}$ consistent with the characteristic accretion rate due to PR drag (BR11; R11a). On the other hand, *PR drag alone is insufficient to explain the highest observed rates* $\dot{M}_Z \sim 10^9$–$10^{11}\,\mathrm{g\,s^{-1}} \gg \dot{M}_{\rm PR,in}$ found in the tail of the distribution in Fig. 1.

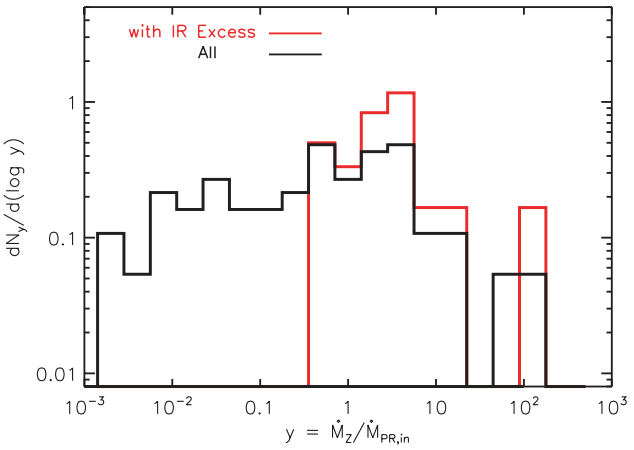

Figure 1. Distribution $\mathrm{d}N_y/\mathrm{d}(\log y)$ of WD metal accretion rates $y \equiv \dot{M}_Z/\dot{M}_{\rm PR,in}$ from the samples of Farihi et al. (2009, 2010b), shown separately for the total population (sample size $N = 62$; black line) and just those systems with detected IR excess (sample size $N = 20$; red line). We normalize the accretion rate $\dot{M}_Z$ to the value $\dot{M}_{\rm PR,in}$ predicted due to optically thick PR drag (equation 43), assuming that $R_\star \simeq 10^9$ cm and using the measured effective temperature of the WD in each system. Note that each distribution has been separately normalized to unity. In Section 5, we show that the current 'observed' accretion rates in systems with $y \gtrsim 1$ and without an IR excess likely overestimate the current real accretion rate (but underestimate the peak accretion rate achieved earlier in their evolution; see Fig. 14).

Rafikov (2011b, hereafter R11b) recently proposed a model for the *coupled* evolution of the solid and gaseous components of WD accretion discs which can in principle explain even these highest accretion rates. The key idea is that a fraction of the gas created at the sublimation radius viscously spreads outwards in order to carry away the angular momentum of the accreting gas (Pringle 1981). The solid and gaseous discs thus overlap at radii $\gtrsim R_s$, providing a natural explanation for their observed radial coincidence (e.g. Melis et al. 2010). Drag forces between the solid and gaseous discs in this region, resulting from their different rotation rates, act to enhance the rate at which solids lose angular momentum and accrete over the rate provided by PR drag alone. This scenario results in a feedback process, and potential 'runaway', because the enhanced rate of solid sublimation increases the accumulation of gas near the sublimation radius, which in turn enhances the strength of drag and rate of solid accretion. Using a local model applied to the evolution of the optically thick disc of solids near its inner radius, R11b showed that during such a runaway $\dot{M}_Z$ can exceed by orders of magnitude the accretion rate $\dot{M}_{\rm PR,in}$ set by PR drag alone.

R11b has shown that the full range of accretion rates in Fig. 1 can in principle be reconciled with the asteroid debris disc model. However, the R11b model is limited by several simplifying assumptions, including its entirely local ('one zone') nature. A more detailed, *global* model of the gaseous and solid disc evolution is necessary to verify and generalize these conclusions.

1.2 This paper

In this paper we present one-dimensional calculations of the coupled evolution of the solid and gaseous components of WD debris discs. Our goal is to test the runaway accretion model of R11b and to begin to address observational tests, such as the expected fraction of metal-bearing WDs with and without observable debris discs and the predicted distribution of accretion rates to compare with data, such as that shown in Fig. 1.

This paper is organized as follows. In Section 2 we overview the model, describing in Section 2.1 our baseline description of the aerodynamic coupling between gaseous and solid discs. In Section 3, we present the equations governing the evolution of the coupled gas and solid discs, including an estimate of characteristic values of the dimensionless parameters of the model (Section 3.4). In Section 4, we present our numerical calculations and describe our results. In Section 5, we present applications of our results. These include a comparison between the true accretion rate and that approximated using the commonly adopted assumption of steady-state accretion (Section 5.1); and predictions for the accretion rate distribution from an ensemble of debris disc systems (Section 5.2). In Section 6, we discuss our results, including a critical assessment of whether the necessary conditions for runaway are achieved in WD debris discs. We also discuss several extensions of our standard model, including the effects of an eccentric gaseous disc (Section 6.1) and the WD

magnetic field (Section 6.2). In Section 7, we provide a summary of our results.

Appendices of this paper contain a number of important auxiliary results, including an evaluation of the role of collisional viscosity in driving the accretion of solids (Appendix A); calculation of the viscous evolution of a disc with a power-law viscosity and mass sources (Appendix B); an analytical derivation of the runaway condition in a simplified but fully global model of disc evolution (Appendix C); and a calculation of the aerodynamic coupling between a solid disc and an *eccentric* gaseous disc (Appendix D). Our results in Appendix B may find useful applications in studies of accretion discs beyond the scope of this work.

2 SUMMARY OF THE MODEL

We now overview the basic model, which is illustrated schematically in Fig. 2. Initially a solid debris disc forms at radii $r \lesssim R_{\rm R} \sim {\rm R}_\odot \sim 10^{11}$ cm from the tidal disruption of a rocky body. We characterize the solid debris disc by its surface density $\Sigma_{\rm d}$ and optical depth

$$\tau_{\rm d} \equiv \frac{\Sigma_{\rm d}}{\Sigma_0}, \qquad \Sigma_0 \equiv \frac{4}{3}\rho_{\rm d} a, \tag{3}$$

where Σ_0 is the fiducial surface density at which $\tau_{\rm d} = 1$, and $\rho_{\rm d} \sim$ a few g cm^{-3} and a are the bulk density and characteristic size, respectively, of disc particles. The initial distribution of solids $\tau_{\rm d}(r)$ depends on the details of the tidal disruption process and on the properties (e.g. mass, composition and tensile strength) and incident orbit of the disrupted body (e.g. Debes, Walsh & Stark 2012). In this work we neglect the important issue of the how the disc forms and circularizes in the first place, which is justified since the time-scale for this process ∼1–100 yr is typically shorter than the other time-scales of relevance (e.g. the viscous time-scale or disc lifetime). However, in Section 6.1 we discuss the effects of eccentricity on the strength of the coupling between solids and gas, which could in principle be relevant to the early phases of disc evolution.

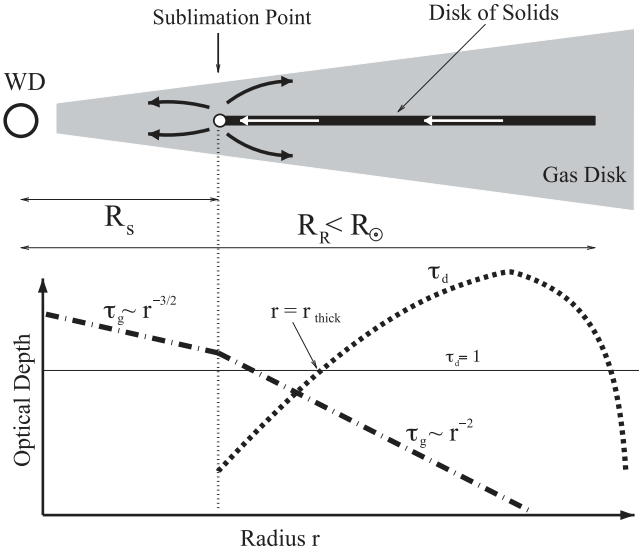

Figure 2. Schematic diagram of the model for WD debris discs described in this paper. An asteroid or other minor body is disrupted by tidal forces inside the Roche radius $R_{\rm R} \sim {\rm R}_\odot$, forming a solid debris disc with surface density distribution $\Sigma_{\rm d}(r) = \Sigma_0 \tau_{\rm d}(r)$ (dashed line), where $\tau_{\rm d}$ is the vertical optical depth (equation 3) as a function of radius r. PR drag transports solids to the sublimation radius $R_{\rm s} \sim 0.2\,{\rm R}_\odot$ (equation 1), where a gaseous disc forms. Turbulent viscosity redistributes the gas surface density $\Sigma_{\rm g} \propto \tau_{\rm g}$ into a steady-state power-law distribution with a break in the slope (see equation B17) at the sublimation radius (dot–dashed line). The gas and solid discs overlap at radii $\gtrsim R_{\rm s}$, resulting in azimuthal aerodynamic drag between the discs which acts to enhance the rate of solid accretion. Our calculations in Section 4 show that drag is most effective at the innermost radius $r \sim r_{\rm thick}$ where the solid disc becomes optically thick ($\tau_{\rm d} \gtrsim 1$). The interaction at this location starts the process which ultimately leads to 'runaway' accretion of the entire solid disc.

Solids accrete inwards, initially due entirely to PR drag, creating gas at the sublimation radius $R_{\rm in} = R_{\rm s} \approx 2 \times 10^{10}$ cm (equation 1). The temperature of the gas $T_{\rm g} \sim 3$–7×10^3 K is higher than that of the solids ($T_{\rm d} < T_{\rm s} \sim 1500$ K) due to differences in their heating and cooling processes (Melis et al. 2010). The aspect ratio of the gaseous disc $h_{\rm g}/r \sim 10^{-3}$ is typically small, but the disc scale-height $h_{\rm g} \sim 10^7$ cm is still much larger than that of the particulate disc, which (with the possible exception of small dust particles) appears to be well settled into the midplane.

Due to angular momentum transport by turbulent viscosity, the gaseous disc accretes both inwards to the WD surface $R_\star \sim 10^9$ cm and spreads outwards to radii $\gtrsim R_{\rm in}$, where it overlaps with the solid disc. If the rate of solid accretion evolves slowly compared to the viscous time, then the gas surface density (proportional to optical depth $\tau_{\rm g}$) develops a power-law radial distribution, with a break in the power-law index at the sublimation radius (see Appendix B). Drag on the solids due to interaction with the gaseous disc enhances the rate of solid accretion.

Note that in this work we do not consider the possibility of gas production due to particle collisions, as suggested by Jura (2008) and Farihi et al. (2009), since, as we demonstrate in Section 6.4, this mechanism cannot maintain the continuous production of metallic gas on a sufficiently long time-scale.

We now discuss one physical mechanism for coupling the dynamics of the solid and gaseous discs: *aerodynamic drag*. As shown later in Section 4, aerodynamic drag is most effective at the innermost radius $r \approx r_{\rm thick}$ where the solid disc becomes optically thick ($\tau_{\rm d} \gtrsim 1$).

2.1 Aerodynamic coupling

The angular velocity of the gaseous disc $\Omega_{\rm g}$ is slightly lower than the Keplerian rate $\Omega_{\rm K} = (GM_\star/r^3)^{1/2}$ at which the solid particles orbit due to the radial pressure gradient in the gaseous disc, $\Omega_{\rm g} - \Omega_{\rm K} \approx (2\Omega_{\rm K} r \rho_{\rm g})^{-1} \partial P_{\rm g}/\partial r$, where $P_{\rm g}$ and $\rho_{\rm g}$ are the midplane gas pressure and density, respectively.[1] This results in an azimuthal velocity difference given by

$$v_{\varphi,{\rm rel}} = -\eta c_{\rm s} \frac{c_{\rm s}}{\Omega r} \approx -200\,{\rm cm\,s^{-1}} \left(\frac{28 m_{\rm p}}{\mu}\right) \left(\frac{T_{\rm g}}{5000\,{\rm K}}\right) \left(\frac{M_\star}{0.6\,{\rm M}_\odot} \frac{R_{\rm in}}{0.2\,{\rm R}_\odot}\right)^{1/2}, \tag{4}$$

where (assuming $c_{\rm s}$ independent of radius)

$$\eta = \frac{1}{2}\left(\frac{3}{2} - \frac{\partial \ln \Sigma_{\rm g}}{\partial \ln r}\right) \tag{5}$$

is a dimensionless parameter set by the radial pressure distribution. Here, $\Sigma_{\rm g} \simeq 2 h_{\rm g} \rho_{\rm g}$ and $h_{\rm g} \simeq c_{\rm s}/\Omega$ are the surface density and vertical scale-height of the gas disc, respectively.

[1] In places hereafter where the distinction between $\Omega_{\rm g}$ and $\Omega_{\rm K}$ is not important, we simply refer to *the* angular rotation rate $\Omega = \Omega_{\rm K} \simeq \Omega_{\rm g}$.

Note that although the total surface density of solids $\Sigma_{\rm d}$ can exceed that of the gas $\Sigma_{\rm g}$ in regions where the two radially overlap, this does not imply that the solids dominate the dynamics of the gas nor eliminate its relative velocity. This is because most of the solid mass is likely locked up in macroscopic particles (with sizes $\sim$ cm; see Graham et al. 1990 and Section 6), which are well settled into the disc midplane, similar to the rings of Saturn. In addition, the gas extends to a much greater vertical height and is not loaded with solids, allowing it rotate at a sub-Keplerian speed due to pressure support. Thus, despite their radial overlap the gas and solid debris are well separated in the vertical direction (see Fig. 2) and there is no tight coupling between them in the sense that the stopping time of the solid particles is much longer than the local orbital period.

The only population of particles that could plausibly be well mixed with the gas are micron-sized silicate particles. However, observationally these represent only a small fraction of the total mass and surface density of the disc: typical values for the total mass are of the order of $\sim 10^{18}$ g (Jura et al. 2009b), resulting in a surface density near the sublimation radius of $\lesssim 10^{-4}$ g cm^{-2}. This is much less than the gas surface density near the sublimation radius, even when the accretion rate equals the maximum value achievable by PR drag (e.g. $\Sigma_{\rm g} \sim 10^{-2}$ g cm^{-2} for $\dot{M}_Z \sim 10^8$ g s^{-1}; see equation 7).

The importance of shear between the solid particles and gaseous disc was first recognized in the context of protoplanetary discs (Whipple 1972) and is now widely believed to result in a variety of important effects, such as the inward migration of solids (Weidenschilling 1977), excitation of turbulence near the disc midplane (e.g. Cuzzi, Dobrovolskis & Champney 1993) and streaming instabilities in the disc of solids (Youdin & Goodman 2005; Johansen et al. 2007).

2.1.1 *Optically thick discs ($\tau_{\rm d} \gtrsim 1$)*

One of the most important (and also most uncertain) issues is the strength of the coupling between the gaseous and solid discs. When the optical depth of the solid disc is high ($\tau_{\rm d} \gg 1$), its geometry may be idealized as that of a solid plate with a zero-slip boundary condition at its surface. In reality, of course, the disc is not a *perfectly smooth* plate; its surface may, for instance, contain structures similar to those observed in the rings of Saturn, such as wakes, vertical particle motions, particle 'pileups' and other highly inhomogeneous small-scale surface density features (Cuzzi et al. 2010). These complications introduce significant uncertainty when calculating the drag force acting on the debris disc.

Even if the idealization of a smooth plate is adopted, one must determine whether the gaseous layer above the plate is laminar or turbulent. A similar issue was first addressed by Goldreich & Ward (1973), who showed that if the gaseous disc remains laminar, then the velocity shear between the two discs is restricted to within the Ekman layer of vertical thickness

$$z_{\rm E} \sim \left(\frac{\nu_{\rm m}}{\Omega}\right)^{1/2} \approx h_{\rm g} \left(\frac{\mu}{\sigma \Sigma_{\rm g}}\right)^{1/2}, \tag{6}$$

where $\nu_{\rm m} \approx \lambda c_{\rm s}/3$ is the *molecular* shear viscosity in the disc (not to be confused with the *turbulent* viscosity ν), $\lambda = \mu/\rho_{\rm g}\sigma$ is the molecular mean free path and σ is the molecular cross-section. The gas surface density near the sublimation radius can be estimated using the expression $\dot{M}_Z = 3\pi\nu\Sigma_{\rm g}$ appropriate for steady-state accretion (e.g. Frank, King & Raine 2002; see also equation B17),

$$\begin{aligned}\Sigma_{\rm g}(r = R_{\rm in}) &\simeq \frac{\dot{M}_Z t_\nu}{3\pi R_{\rm s}^2} \\ &\approx 3 \times 10^{-3}\,{\rm g\,cm^{-2}} \left(\frac{\dot{M}_Z}{10^8\,{\rm g\,s^{-1}}}\right) \left(\frac{\alpha}{10^{-3}}\right)^{-1} \\ &\quad \times \left(\frac{R_{\rm s}}{0.2\,{\rm R_\odot}}\right)^{-3/2}, \end{aligned} \tag{7}$$

where we have assumed $R_{\rm in} \approx R_{\rm s}$ and have substituted equation (2) for $t_\nu = R_{\rm s}^2/\nu$, adopting fiducial parameters of $\mu = 28 m_{\rm p}$, $T_{\rm g} = 5000$ K and $M_\star = 0.6\,{\rm M_\odot}$.

For $\sigma \approx 10^{-15}$ cm^{-2}, $\alpha = 10^{-3}$ and the typical range of measured WD accretion rates $\dot{M}_Z \sim 10^8$–10^{10} g s^{-1}, equation (6) shows that the Ekman layer thickness $z_{\rm E} \sim 10^3$–10^5 cm is generally much smaller than the disc scale-height of $h_{\rm g} \sim 10^7$ cm. For the same parameters, the Reynolds number of the Ekman layer is estimated to be

$$Re_{\rm E} = \frac{v_{\varphi,{\rm rel}} z_{\rm E}}{\nu_{\rm m}} \approx \frac{h_{\rm g}}{r} \left(\frac{\sigma \Sigma_{\rm g}}{\mu}\right)^{1/2} \sim 0.1\text{–}1. \tag{8}$$

Under terrestrial conditions, both numerical calculations (Coleman, Ferziger & Spalart 1990) and experiments (Faller 1963) find that $Re_{\rm E} \gtrsim 10^2$ is necessary for the Ekman layer to become turbulent. At first glance it thus appears that the gas layer above the debris disc is laminar.

In astrophysical discs, however, the Ekman layer may be susceptible to Kelvin–Helmholtz (KH) instabilities (Goldreich & Ward 1973). If one assumes momentarily that fluid in the shear layer is incompressible ($v_{\varphi,{\rm rel}} \ll c_{\rm s}$), then the Richardson number of the Ekman layer is given by

$$Ri_{\rm E} = -g_z \frac{\partial \ln \rho/\partial z}{(\partial v_\varphi/\partial z)^2} \sim \left(\frac{g_z z_{\rm E}}{c_{\rm s} v_{\varphi,{\rm rel}}}\right)^2 \approx \left(\frac{\Omega r}{c_{\rm s}} \frac{\mu}{\sigma \Sigma_{\rm g}}\right)^2, \tag{9}$$

where $g_z \simeq GM_\star z_{\rm E}/r^3$ is the vertical gravitational acceleration near the midplane and we have made the approximations $\partial \ln \rho/\partial z \sim g_z/c_{\rm s}^2$ and $\partial v_\varphi/\partial z \sim v_{\varphi,{\rm rel}}/z_{\rm E}$. Again adopting the fiducial parameters and range of accretion rates given above, one finds $Ri_{\rm E} \sim 10^{-2}$–10^{-6}, indicating that the flow is grossly KH unstable and must be turbulent.[2]

If the flow over the disc surface is turbulent, then the force per unit surface area is given by (Goldreich & Ward 1973)

$$f_a(\tau_{\rm d} \gtrsim 1) = -{\rm Re}_\star^{-1} \rho_{\rm g} v_{\varphi,{\rm rel}} |v_{\varphi,{\rm rel}}|, \tag{10}$$

where ${\rm Re}_\star^{-1}$ is a proportionality constant. Estimates of the value of ${\rm Re}_\star$ in the case of a smooth solid plate vary significantly in the literature, ranging from ${\rm Re}_\star \approx 20$ (Dobrovolskis, Dacles-Mariani & Cuzzi 1999) to ${\rm Re}_\star \approx 500$ (Goldreich & Ward 1973). Even given this uncertainty, the smooth plate model probably underestimates the true drag, since the surface of a particulate disc is not continuous. As we describe below, in some cases the gas–solid interaction may be better described as that due to a combination of individual particles, in which case the effective value of ${\rm Re}_\star$ may be much smaller.

2.1.2 *Optically thin discs ($\tau_{\rm d} \lesssim 1$)*

In the opposite limit of an extremely optically thin disc ($\tau_{\rm d} \ll 1$), debris particles interact with the gas individually. The speed of

[2] A similar conclusion does not apply under terrestrial conditions because $Ri_{\rm E} \propto g_z^2$ and the gravitational acceleration on Earth is $\gtrsim 10^4$ times higher than g_z in WD debris discs.

gas relative to solids in this case is just $v_{\varphi,\rm rel}$ (equation 4), since the particles do not disturb the mean gas flow appreciably. The drag force per unit surface area for optically thin discs is then

$$f_a(\tau_{\rm d} \ll 1) = \frac{\Sigma_{\rm d}}{(4\pi/3)\rho_{\rm d} a^3} F_{\rm D} = \tau_{\rm d} \frac{F_{\rm D}}{\pi a^2}, \tag{11}$$

where $F_{\rm D}$ is the drag force on an individual particle of size a.

The magnitude of $F_{\rm D}$ depends on two key parameters (Whipple 1972; Weidenschilling 1977): (1) the ratio of particle size a to the molecular mean-free path λ,

$$\frac{a}{\lambda} = \frac{\Sigma_{\rm g}\Omega a}{2\mu c_{\rm s}} \sim 5 \left(\frac{\dot{M}_Z}{10^8\,{\rm g\,s^{-1}}}\right)\left(\frac{\alpha}{10^{-3}}\right)^{-1}\left(\frac{a}{\rm cm}\right), \tag{12}$$

and (2) the *particle* Reynolds number

$$Re_{\rm p} = \frac{2a v_{\varphi,\rm rel}}{\nu_{\rm m}} \sim \frac{c_{\rm s}}{\Omega r}\frac{a}{\lambda} \sim 10^{-2}\left(\frac{\dot{M}_Z}{10^8\,{\rm g\,s^{-1}}}\right)\left(\frac{\alpha}{10^{-3}}\right)^{-1}\left(\frac{a}{\rm cm}\right), \tag{13}$$

where in equation (12) we have substituted equation (7) for $\Sigma_{\rm g}$, and in our numerical estimates we again adopt characteristic values for the relevant parameters at $r \sim R_{\rm s}$.

Equation (13) shows that $Re_{\rm p} \lesssim 1$ is satisfied for $\alpha = 10^{-3}$ and the range of accretion rates $\dot{M}_Z \sim 10^8$–10^{10} g cm^{-3} provided that the typical particle size obeys $a \lesssim$ 1–100 cm. Assuming that this condition is indeed satisfied (consistent with observations; Graham et al. 1990; see also Section 6), then the interaction of gas with *individual particles* is in the laminar regime. The drag force in this case, in the Stokes ($a \gtrsim \lambda$) and Epstein ($a \lesssim \lambda$) regimes, respectively, is given by the expression

$$F_{\rm D} = \begin{cases} 6\pi a \rho_{\rm g} \nu_{\rm m} v_{\varphi,\rm rel}, & a \gtrsim \lambda \text{ (Stokes)}, \\ (4\pi/3)\rho_{\rm g} a^2 c_{\rm s} v_{\varphi,\rm rel}, & a \lesssim \lambda \text{ (Epstein)}. \end{cases} \tag{14}$$

These two limits are readily combined into a single formula

$$F_{\rm D} = -\frac{12\pi a^2}{Re_{\rm p}} \rho_{\rm g} v_{\varphi,\rm rel} |v_{\varphi,\rm rel}| \times \min\left(1, \frac{2}{3}\frac{a}{\lambda}\right), \tag{15}$$

which substituted into equation (11) gives the force per area

$$f_a(\tau_{\rm d} \ll 1) = -\frac{12}{Re_{\rm p}} \tau_{\rm d} \rho_{\rm g} v_{\varphi,\rm rel} |v_{\varphi,\rm rel}| \times \min\left(1, \frac{2}{3}\frac{a}{\lambda}\right). \tag{16}$$

2.1.3 *Connecting the optically thin and optically thick regimes*

A comparison of our expressions for the drag force in the optically thick (equation 10) and optically thin (equation 16) regimes shows that they do not match smoothly at $\tau_{\rm d} \sim 1$, since in general one expects ${\rm Re}_\star^{-1} \ll 1 \ll 12/Re_{\rm p}$, while $Re_{\rm p} \propto a/\lambda$ varies independently. This mismatch is not unexpected, since the transition regime $\tau_{\rm d} \sim 1$ is precisely where the smooth-plate approximation breaks down. In reality, there is an intermediate range of optical depths, between $\tau_{\rm d} \sim 1$ and some lower value $\tau_{\rm d} \equiv \tau_{\rm d,ind} \ll 1$, between which the solid–gas coupling is not well described as either drag on a *continuous* entity, nor as the sum of *incoherent* forces on individual particles. The relative velocity between the gas and particle disc in this regime also lies somewhere between zero (the no-slip boundary condition realized in the case of a smooth plate) and $v_{\varphi,\rm rel}$ (equation 4).

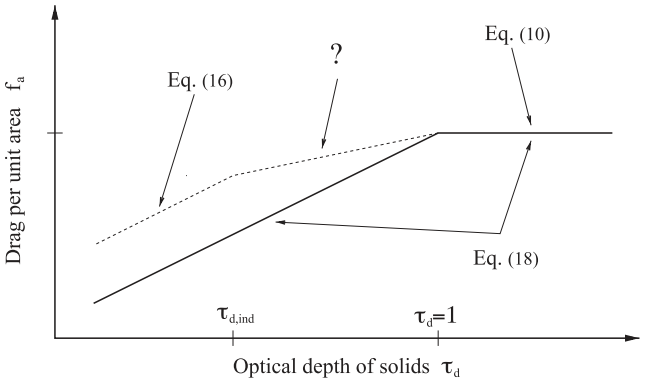

Figure 3. Different regimes of aerodynamic drag between the gaseous and particulate discs as a function of the optical depth of solids $\tau_{\rm d}$. The drag law used in this work (solid line; equation 16) underestimates the drag force f_a in the optically thin limit $\tau_{\rm d} \lesssim 1$ as compared to the realistic drag law shown by the dashed line, although its qualitative behaviour is captured. The true coupling between gas and solids is poorly understood at intermediate values of the optical depth $\tau_{\rm d,ind} \lesssim \tau_{\rm d} \lesssim 1$, at which collective effects influence aerodynamic drag. See text for details.

In this work we do not model this poorly understood intermediate regime of gas–particle interaction in detail. Instead we adopt the following simple formula for the drag force, which interpolates smoothly between optically thick and optically thin limits:

$$f_a = -\frac{1 - {\rm e}^{-\tau_{\rm d}}}{{\rm Re}_\star} \rho_{\rm g} v_{\varphi,\rm rel} |v_{\varphi,\rm rel}| \tag{17}$$

$$= \eta |\eta| A_a \Sigma_{\rm g} \left(1 - {\rm e}^{-\tau_{\rm d}}\right), \tag{18}$$

where

$$A_a = {\rm Re}_\star^{-1} \frac{c_{\rm s}^3}{\Omega r^2}. \tag{19}$$

Although equation (17) reduces to equation (10) when $\tau_{\rm d} \gtrsim 1$, it considerably underestimates the drag force for $\tau_{\rm d} \ll 1$ as compared to equation (16). This point is illustrated in Fig. 3, in which we compare our approximation of the drag force in equation (17) to a schematic representation of the more realistic drag behaviour, which properly reduces to equations (10) and (16) in the optically thick ($\tau_{\rm d} \gtrsim 1$) and thin ($\tau_{\rm d} \lesssim \tau_{\rm d,ind}$) limits, respectively. Although there are modest differences between these expressions at small values of $\tau_{\rm d}$, equation (17) nevertheless does reproduce the qualitative scaling $f_a \propto \tau_{\rm d}$ in the optically thin regime, which is the most important property for the purposes of our current work. As we describe in Section 4, this distinction between 'weak' ($\tau_{\rm d} \lesssim 1$) and 'strong' ($\tau_{\rm d} \gtrsim 1$) coupling has an important role in the build-up to runaway in the accretion disc evolution.

Although our numerical calculations focus on aerodynamic coupling of the above form, in principle other forms of drag may be present, such as enhanced drag due to an eccentric gas disc (Section 6.1). To the extent that the drag force remains proportional to the local gas mass, an expression of the form in equation (18) may be applicable to these cases as well, provided that an appropriate alternative expression is substituted for equation (19).

3 COUPLED EVOLUTION OF THE PARTICULATE AND GASEOUS DISCS

In this section we present the equations governing the solid and gaseous discs, including their angular momentum exchange due to aerodynamic drag and mass exchange due to sublimation.

3.1 Solid disc

The evolution of the solid disc obeys the continuity equation

$$\frac{\partial \Sigma_{\rm d}}{\partial t} - \frac{1}{2\pi r}\frac{\partial \dot{M}}{\partial r} = S_{\rm d}, \tag{20}$$

where $\dot{M}$ is the mass flux through the solid disc and the function $S_{\rm d}$ accounts for sources or sinks of solid mass, such as dust sublimation or gas condensation.

The mass flux consists of several components

$$\dot{M} = \dot{M}_{\rm PR} + \dot{M}_a + \dot{M}_{\rm d}, \tag{21}$$

which include the mass flux due to PR drag (R11a)

$$\dot{M}_{\rm PR} = \zeta \frac{L_\star}{c^2}\left(1 - {\rm e}^{-\tau_{\rm d}/\zeta}\right), \tag{22}$$

where (Friedjung 1985)

$$\zeta(r) = \frac{4}{3\pi}\frac{R_\star}{r} \tag{23}$$

is the incidence angle of the stellar radiation with respect to the flat disc midplane. Note that $\dot{M}_{\rm PR}$ depends on the optical depth $\tau_{\rm d}/\zeta$ to stellar light arriving at grazing incidence angle $\zeta \ll 1$.

A second contribution to the mass flux results from aerodynamic drag by the gas disc (R11b):

$$\dot{M}_a = \frac{4\pi r f_a}{\Omega} = \frac{4\pi\eta|\eta| r A_a \Sigma_{\rm g}}{\Omega}\left(1 - {\rm e}^{-\tau_{\rm d}}\right), \tag{24}$$

where we have substituted equation (17) for f_a from Section 2.1. The factor A_a in equation (24) depends on the specific form of aerodynamic drag. In general, we assume that this function scales as a power law with radius

$$A_a = A_{\rm in}\left(\frac{r}{R_{\rm in}}\right)^{\kappa}, \tag{25}$$

where κ is a constant that depends on the drag law. If $c_{\rm s}$ is constant with radius, our fiducial drag law given in equation (17) implies $\kappa = -1/2$, a value we therefore adopt throughout the remainder of this paper.

From equation (24) one can define the *sublimation* time $t_{\rm s}$ as the time-scale on which the characteristic gaseous mass near the sublimation radius $\pi R_{\rm in}^2 \Sigma_{\rm g}$ is replenished by accretion due to aerodynamic drag (in the optically thick regime $\tau_{\rm d} \gg 1$) alone:

$$t_{\rm s} \equiv \frac{\pi R_{\rm in}^2 \Sigma_{\rm g}}{\dot{M}_a(r = R_{\rm in}, \tau_{\rm d} \gg 1)} = \frac{\Omega_{\rm in} R_{\rm in}}{4A_{\rm in}}, \tag{26}$$

where $\Omega_{\rm in} \equiv \Omega(R_{\rm in})$ and in evaluating $\dot{M}_a$ (equation 24) we have set $\eta = 1$. Note that this time-scale is independent of $\Sigma_{\rm g}$.

The final contribution to the mass flux $\dot{M}_{\rm d}$ in equation (21) accounts for the possible condensation of gas. This process necessarily exchanges angular momentum between the gas and solid discs, thus driving additional solid accretion. In this paper we neglect condensation by setting $S_{\rm d} = \dot{M}_{\rm d} = 0$ (see Section 6.3). However, once an expression for $S_{\rm d}$ is given, the resulting expression for $\dot{M}_{\rm d}$ is easily calculable.

3.2 Gaseous disc

The gaseous disc also evolves according to the continuity equation (Lin & Papaloizou 1996)

$$\frac{\partial \Sigma_{\rm g}}{\partial t} - \frac{1}{r}\frac{\partial}{\partial r}\left[3r^{1/2}\frac{\partial}{\partial r}\left(\Sigma_{\rm g}\nu r^{1/2}\right) - \frac{2\Sigma_{\rm g}\Lambda}{\Omega}\right] = S_{\rm g}, \tag{27}$$

where ν is again the turbulent viscosity and

$$\Sigma_{\rm g}\Lambda = \eta|\eta| A_a \Sigma_{\rm g} r\left(1 - {\rm e}^{-\tau_{\rm d}}\right) \tag{28}$$

is the torque per unit area on the gaseous disc due to the back-reaction from the aerodynamic drag force f_a (equation 17) acting on the solid disc. In Appendix C, we explore a global model with back-reaction neglected ($\Lambda = 0$) and demonstrate that the main evolutionary features are still preserved even in this simplified set-up.

The function $S_{\rm g}$ represents sources and sinks of gaseous mass. The most important source of gas is that due to sublimation, which we assume is sharply localized at $r = R_{\rm in}$ and is proportional to the rate of solid accretion $\dot{M}$:

$$S_{\rm g} = \frac{\dot{M}(r = R_{\rm in})}{2\pi R_{\rm in}}\delta(r - R_{\rm in}), \tag{29}$$

where $\delta(z)$ is the Dirac delta function.

We assume that the gas temperature and sound speed are independent of radius, in which case the turbulent viscosity may be written as

$$\nu(r) = \alpha c_{\rm s} h_{\rm g} = \alpha(r)\frac{c_{\rm s}^2}{\Omega_{\rm in}}\left(\frac{r}{R_{\rm in}}\right)^{3/2}, \tag{30}$$

where in general we allow the dimensionless α-parameter to vary with radius, denoting $\alpha_{\rm in} \equiv \alpha(r = R_{\rm in})$.

3.3 Dimensionless equations

We now bring the equations from the previous two sections into dimensionless form. We first introduce several new definitions:

$$\tilde{t} \equiv \frac{t}{t_\nu}, \quad x \equiv \frac{r}{R_{\rm in}}, \quad \tau_{\rm g} \equiv \frac{\Sigma_{\rm g}}{\Sigma_0}, \quad \zeta_{\rm in} \equiv \frac{4}{3\pi}\frac{R_\star}{R_{\rm in}}, \tag{31}$$

$$s_{\rm g} \equiv \frac{S_{\rm g} t_\nu}{\Sigma_0}, \quad \dot{M}_{\rm PR,in} \equiv \frac{L_\star}{c^2}\zeta_{\rm in}, \quad \tilde{\alpha}(x) \equiv \frac{\alpha(x)}{\alpha_{\rm in}}, \tag{32}$$

$$\dot{m} \equiv \frac{\dot{M} t_{\rm s}}{\pi R_{\rm in}^2 \Sigma_0}, \quad \dot{m}_{\rm d} \equiv \frac{\dot{M}_{\rm d} t_{\rm s}}{\pi R_{\rm in}^2 \Sigma_0}, \tag{33}$$

noting in particular that we express time in units of the viscous time t_ν at $R_{\rm in}$ (equation 2) and radius in units of the location of the inner edge of the solid disc $R_{\rm in} \simeq R_{\rm s}$ (equation 1).

We also introduce two key parameters: the *feedback parameter*

$$\mathcal{F} \equiv \frac{t_\nu}{t_{\rm s}} = \frac{4A_{\rm in}R_{\rm in}}{\alpha_{\rm in}c_{\rm s}^2}, \tag{34}$$

and the *PR parameter*

$$b_{\rm PR} \equiv \frac{\dot{M}_{\rm PR,in} t_{\rm s}}{\pi R_{\rm in}^2 \Sigma_0}. \tag{35}$$

As we will show in Section 4, the feedback parameter has an important qualitative effect on the evolution of WD debris discs, in particular by controlling whether and when runaway accretion occurs. The physical interpretation of the PR parameter is less clear, but roughly speaking it represents the ratio of the time-scale for disc replenishment due to the gas drag-assisted accretion of solids

t_s (equation 26) to the time-scale on which the gas disc can be replenished by PR drag alone, given a marginally optically thick disc (mass $\approx \pi R_{\rm in}^2 \Sigma_0$) concentrated near the sublimation radius. Note that (1) $b_{\rm PR}$ depends on Σ_0 (equation 3) and is thus sensitive to the particle size a, and (2) from equations (33) and (35) it follows that $\dot{M} = \dot{M}_{\rm PR,in}\dot{m}/b_{\rm PR}$.

Given these definitions, we now recast the evolutionary equations from Sections 3.1 and 3.2 in dimensionless form. First, the evolution of the solid disc (equation 20) can be written as

$$\frac{\partial \tau_{\rm d}}{\partial \tilde{t}} - \frac{\mathcal{F}}{2}\frac{1}{x}\frac{\partial \dot{m}_{\rm d}}{\partial x} = 0, \tag{36}$$

where the various contributions to the mass flux of solids are now

$$\dot{m}_{\rm d} = \dot{m}_a + \dot{m}_{\rm PR}, \tag{37}$$

$$\dot{m}_a = \eta|\eta|\tau_{\rm g} x^{(5/2)+\kappa}\left(1 - {\rm e}^{-\tau_{\rm d}}\right), \tag{38}$$

$$\dot{m}_{\rm PR} = b_{\rm PR} x^{-1}\left(1 - {\rm e}^{-\tau_{\rm d} x/\zeta_{\rm in}}\right), \tag{39}$$

with

$$\eta = \frac{1}{2}\left(\frac{3}{2} - \frac{\partial \ln \tau_{\rm g}}{\partial \ln x}\right). \tag{40}$$

The evolution of the gaseous disc (equation 27) can now be written as

$$\frac{\partial \tau_{\rm g}}{\partial \tilde{t}} - \frac{1}{x}\frac{\partial}{\partial x}\left[3x^{1/2}\frac{\partial}{\partial x}\left(\tau_{\rm g}\tilde{\alpha}x^2\right) - \frac{\mathcal{F}}{2}\dot{m}_a\right] = s_{\rm g}, \tag{41}$$

with the sublimation source term (equation 29)

$$s_{\rm g} = \frac{\mathcal{F}}{2}\dot{m}_{\rm d}(x=1)\delta(x-1). \tag{42}$$

The above expressions represent a system of two equations (36) and (41) for two unknown functions $\tau_{\rm d}$ and $\tau_{\rm g}$ and x and $\tilde{t}$, with three independent parameters – $\mathcal{F}$, $b_{\rm PR}$ and $\zeta_{\rm in}$ – and two functions of x that must be independently supplied – $\tilde{\alpha}(x)$ and $A(x)$ (or κ).

3.4 Characteristic values of key parameters

We now estimate characteristic values of the key parameters in our model, which are useful for scaling our solutions in Section 4 to arbitrary physical situations.

First, we estimate the characteristic accretion rate set by PR drag under optically thick conditions (equation 32)

$$\dot{M}_{\rm PR,in} = \frac{L_\star}{c^2}\zeta_{\rm in} \approx 7\times 10^7\,{\rm g\,s^{-1}}\left(\frac{R_\star}{0.01\,{\rm R_\odot}}\frac{T_\star}{10^4\,{\rm K}}\frac{T_{\rm s}}{1500\,{\rm K}}\right)^2, \tag{43}$$

where $\zeta_{\rm in} = 4R_\star/3\pi R_{\rm in}$ (equation 31), $L_\star = 4\pi R_\star^2\sigma_{\rm sb}T_\star^4$ and we have again assumed $R_{\rm in} = R_{\rm s}$.

Using our fiducial model for aerodynamic drag given in equation (19), the feedback parameter (equation 34) can be written as

$$\begin{aligned}\mathcal{F} &= \frac{4}{{\rm Re}_\star\alpha_{\rm in}}\frac{c_{\rm s}}{\Omega_{\rm in}R_{\rm in}}\\ &\approx 7{\rm Re}_\star^{-1}\left(\frac{\alpha_{\rm in}}{10^{-3}}\right)^{-1}\left(\frac{T_{\rm g}}{5000\,{\rm K}}\right)^{1/2}\left(\frac{M_\star}{0.6\,{\rm M_\odot}}\right)^{-1/2}\\ &\quad\times\left(\frac{R_\star}{0.2\,{\rm R_\odot}}\right)^{1/2}.\end{aligned} \tag{44}$$

Depending on the uncertain value of ${\rm Re}_\star \sim 1-100$ (see discussion in Section 2.1.1), equation (44) shows that strong feedback $\mathcal{F} \gtrsim 1$ requires a rather low value of the viscosity $\alpha_{\rm in} \lesssim 10^{-2}$–$10^{-4}$ at the sublimation radius. We will discuss the value of $\mathcal{F}$ in actual debris disc systems further in Section 6.

Finally, we estimate characteristic values of the PR parameter $b_{\rm PR}$ (equation 35):

$$\begin{aligned}b_{\rm PR} &= \frac{4}{\pi}\mathcal{F}^{-1}\frac{\sigma_{\rm sb}(GM_\star)^{1/2}}{c^2\rho_{\rm d}}\frac{R_\star^3}{R_{\rm in}^{5/2}}\frac{T_\star^4}{\alpha c_{\rm s}^2 a}\\ &\approx 3\times 10^{-3}\mathcal{F}^{-1}\left(\frac{\alpha_{\rm in}}{10^{-3}}\right)^{-1}\left(\frac{a}{\rm cm}\right)^{-1}\left(\frac{R_{\rm in}}{0.2\,{\rm R_\odot}}\right)^{-5/2}\\ &\quad\times\left(\frac{T_\star}{10^4\,{\rm K}}\right)^4\left(\frac{R_\star}{0.01\,{\rm R_\odot}}\right)^3\left(\frac{M_\star}{0.6\,{\rm M_\odot}}\right)^{1/2}\\ &\quad\times\left(\frac{\mu}{28m_{\rm p}}\right)\left(\frac{\rho_{\rm d}}{2.5\,{\rm g\,cm^{-3}}}\right)^{-1},\end{aligned} \tag{45}$$

where we have used the definitions for $\dot{M}_{\rm PR,in}$ (equation 32), Σ_0 (equation 3), $\mathcal{F}$ (equation 34) and $R_{\rm s}$ (equation 1). Note that the above estimate is independent of the specific model for aerodynamic drag, except implicitly through the value of $\mathcal{F}$. Although $b_{\rm PR} \propto R_{\rm in}^3 T_\star^4$ appears to depend sensitively on the WD effective temperature and the inner radius of the solid disc, if the latter coincides with the sublimation radius $R_{\rm in} \approx R_{\rm s} \propto R_\star T_\star^2$ (equation 1) then the dependence becomes less sensitive, $b_{\rm PR} \propto R_\star^{1/2}T_\star^{-1}$.

Equation (45) shows that for typical ranges in the values of the most uncertain parameters $a \sim 0.1-10\,{\rm cm}$ and $\alpha_{\rm in} \sim 10^{-4}-10^{-3}$ under conditions of positive feedback $\mathcal{F} > 1$, one finds relatively small characteristic values $b_{\rm PR} \sim 10^{-4}-1$. Note that a low value of $b_{\rm PR}$ increases $\dot{M}/\dot{M}_{\rm PR,in}$ for a given $\dot{m}$ (see the text after equation 35).

4 NUMERICAL CALCULATIONS

In this section we present our numerical calculations of WD debris disc evolution.

4.1 Technical preliminaries

We evolve the gas surface density $\tau_{\rm g}$ (equation 41) using the 2N-RK3 scheme described in Brandenburg (2003). The solid surface density $\tau_{\rm d}$ (equation 36) is evolved as described in BR11. The gas and solid evolution are coupled at each timestep by the aerodynamic torque $\propto \dot{m}_a$ (equation 38) and the point source of gas due to sublimation $\propto s_{\rm g}$ (equation 42). We adopt a logarithmic radial grid that extends from a location near the WD surface ($x = 0.2$) out to a radius that at all times safely exceeds the outer edge of the solid distribution ($x = 20$). In most cases the number of radial grid cells is taken to be 100; we have verified that our results are independent of resolution by repeating select additional calculations with higher resolution.

The initial gas density is set equal to zero at all radii, $\tau_{\rm g}(x, t=0) = 0$, while different initial distributions (e.g. 'Gaussian ring' and 'top-hat') are adopted for the dust surface density, as described below. The inner boundary condition on $\tau_{\rm g}$ is set to enforce a constant mass accretion rate $\propto \Sigma_{\rm g}\nu$ across the ghost zones using the value in the first active zone, while $\tau_{\rm g}$ is interpolated across the outer boundary. We confirm that our results are insensitive to the precise boundary conditions adopted. We have also verified that the code conserves total mass and angular momentum by checking that any decreases in their values with time are compensated by their fluxes across the inner grid cell (see Metzger, Piro & Quataert 2009).

4.2 Fiducial dimensional model

In what follows, we present our results both in dimensionless form and, for purposes of clarity, in dimensional units assuming fiducial parameters for the properties of the WD and debris disc. In our fiducial model we assume a WD with mass $M_\star = 0.6\,\mathrm{M}_\odot$, radius $R_\star = 0.01\,\mathrm{R}_\odot$ and surface temperature $T_\star = 10^4\,\mathrm{K}$, such that the sublimation radius is $R_\mathrm{s} \simeq 0.2\,\mathrm{R}_\odot$ and the maximum accretion rate due to PR drag is $\dot{M}_\mathrm{PR,in} \simeq 10^8\,\mathrm{g\,s^{-1}}$ (equation 43). For purposes of calculating the disc surface density (equation 3) we assume a typical particle density $\rho_\mathrm{d} = 2.5\,\mathrm{g\,cm^{-3}}$ and size $a = 1\,\mathrm{cm}$. Finally, in calculating the viscous time-scale (equation 2) we assume the dimensionless viscosity to be $\alpha_\mathrm{in} = 10^{-3}$.

4.3 Optically thin ring

We begin by considering the evolution of a thin ring of solid debris with an initial radial profile of the form

$$\tau_\mathrm{d}(x, t = 0) = \tau_{\mathrm{d},0} \exp\left[-\frac{(x - x_0)^2}{(\Delta x)^2}\right], \tag{46}$$

where $x_0 > 1$ and Δx specify the ring centre and its radial thickness, respectively. Although the distribution of solid debris following the tidal disruption of an asteroid may not be well described by a Gaussian ring, we focus initially on this simple distribution because it allows us to explore the dependence of the disc evolution on the characteristic optical depth and location of the solid material. In physical units, the total mass in the initial disc is given by

$$\begin{aligned} M_\mathrm{tot} &= \int_{R_\mathrm{in}}^{\infty} 2\pi r \Sigma_\mathrm{d} \mathrm{d}r \approx \pi (x_0 R_\mathrm{in})^2 (\Delta x / x_0) \Sigma_0 \tau_{\mathrm{d},0} \\ &\approx 10^{21}\,\mathrm{g}\ \tau_{\mathrm{d},0} \left(\frac{\Delta x}{x_0}\right) \left(\frac{a}{\mathrm{cm}}\right) \left(\frac{x_0}{5}\right)^2, \end{aligned} \tag{47}$$

where we have used the definition $\Sigma_0 = (4/3)\rho_\mathrm{d} a$ (equation 3) and have assumed characteristic values for $R_\mathrm{s} = 0.2\,\mathrm{R}_\odot$ and $\rho_\mathrm{d} = 2.5\,\mathrm{g\,cm^{-3}}$.

Fig. 4 shows our calculation of the evolution of an *optically thin* ring with $\tau_{\mathrm{d},0} = 10^{-3}$, $x_0 = 5$ and $\Delta x = 0.5$, corresponding to $M_\mathrm{tot} = 10^{17}\,\mathrm{g}$ for $a = 1\,\mathrm{cm}$. Note that in this example the solid disc is optically thin both in the vertical direction ($\tau_\mathrm{d} \ll 1$) and horizontally to the incident stellar radiation, for which the condition $\tau_\parallel \equiv \tau_\mathrm{d}/\zeta \ll 1$ is instead relevant (see equation 22 and surrounding discussion). We adopt typical values for the parameters $b_\mathrm{PR} = 10^{-2}$ (equation 45), $\zeta_\mathrm{in} = 0.04$ (equation 23) and $\mathcal{F} = 10$ (equation 44), the last allowing for the possibility of strong gas–solid feedback. Solid and dashed lines show the radial distribution of τ_d and τ_g, respectively, at several times $t = 0, 3, 10,$ and 30 (in units of the viscous time t_ν at $x = 1$) with different colours. Fig. 5 shows the gas accretion rate at the inner boundary $\dot{M}_Z \equiv \dot{M}(x = 0)$ in units of the optically thick PR rate $\dot{M}_\mathrm{PR,in}$ (equation 32).

Figs 4 and 5 illustrate that the evolution of τ_d is very similar to the case without gas drag, as explored previously by BR11. BR11 show that when the disc is optically thin with $\tau_\mathrm{d}/\zeta < 1$ at all radii (as satisfied in this case), the dust at radius x accretes on a characteristic time-scale set by PR drag

$$t_\mathrm{acc,thin} \approx \frac{\pi r^2 \Sigma_\mathrm{d}}{\dot{M}_\mathrm{PR}(\tau_\mathrm{d}/\zeta \ll 1)} = \frac{\pi r^2 \Sigma_0}{\dot{M}_\mathrm{PR,in} \zeta_\mathrm{in}^{-1}} = \frac{\zeta_\mathrm{in} x^2}{b_\mathrm{PR} \mathcal{F}} t_\nu, \tag{48}$$

where $\dot{M}_\mathrm{PR}(\tau_\mathrm{d}/\zeta \ll 1) \simeq L_\star \tau_\mathrm{d}/c^2 = \dot{M}_\mathrm{PR,in} \tau_\mathrm{d} \zeta_\mathrm{in}^{-1}$ is the accretion rate due to PR drag in the optically thin limit (equation 22) and we have used the definitions in equations (23), (34) and (35) for the dimensionless parameters ζ_in, $\mathcal{F}$ and b_PR respectively. Note that although we scale $t_\mathrm{acc,thin}$ to the viscous time in equation (48) to compare most easily with our numerical results, we emphasize that the accretion time in the optically thin case depends solely on the rate of PR drag when $t_\mathrm{acc,thin} \gtrsim t_\nu$.

As time advances, the solid ring thus drifts inwards and broadens, the latter simply because the accretion time-scale $t_\mathrm{acc,thin}$ decreases $\propto x^2$, consistent with the evolution of τ_d in Fig. 4. Substituting the relevant parameters, equation (48) predicts that most of the solids reach $x = 1$ on a time-scale of $t_\mathrm{acc,thin}(x = x_0) \approx 10\,t_\nu$ which is set by the initial peak of the dust distribution $x \approx x_0 = 5$. This estimate agrees well with the time-scale that the gas accretion peaks in our

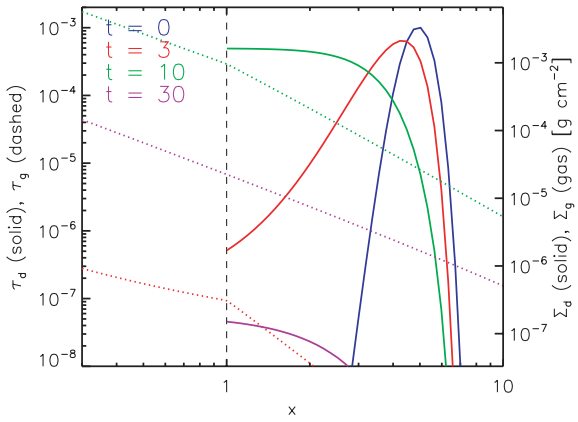

Figure 4. Evolution of the surface density profiles of solids (τ_d; solid lines) and gas (τ_g; dotted lines), assuming an initially optically thin ring of solids ($\tau_{\mathrm{d},0} = 10^{-3}$) concentrated at $x_0 = 5$ (equation 46). Snapshots are shown at several times $t = 0$ (blue), $t = 3$ (red), $t = 10$ (green) and $t = 30$ (purple) in units of the viscous time t_ν at the sublimation radius $x = 1$ (vertical dashed line). The calculation assumes typical values for the parameters $b_\mathrm{PR} = 10^{-2}$, $\zeta_\mathrm{in} = 0.04$ and $\mathcal{F} = 10$. Note that the evolution of τ_d is very similar to the case without gas drag studied by BR11, even though the level of feedback is high ($\mathcal{F} \gg 1$). At times when the sublimation rate evolves slowly, the evolution of τ_g is well described by the broken power law, as predicted by the analytic steady-state solution to the viscous diffusion equation in the presence of a point source of gas at $x = 1$ (see Appendix B). In plotting dimensional units we have adopted a fiducial WD debris disc model (Section 4.2).

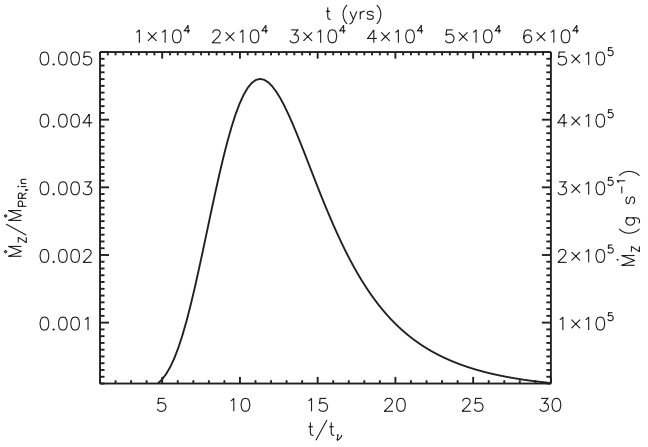

Figure 5. Gas accretion rate on to the WD surface $\dot{M}_Z \equiv \dot{M}(x = 0)$ in units of $\dot{M}_\mathrm{PR,in}$ (equation 32) as a function of time for the calculation shown in Fig. 4. The accretion rate peaks on a time-scale of $t_\mathrm{peak} \approx 10\,t_\nu$ that is well approximated by the analytic estimate in equation (48). In plotting dimensional units we have adopted a fiducial WD debris disc model (Section 4.2).

solution (Fig. 5), as is expected because the gas accretion rate at the origin faithfully tracks the rate of solid sublimation when the latter varies on time-scales greater than the viscous time t_ν.

We conclude that gas coupling does not significantly affect the evolution of optically thin debris discs. We have confirmed this by running an otherwise identical calculation with the gas coupling turned off, i.e. artificially setting the term $\dot{M}_a = 0$. We find a negligible difference between the solutions with and without gas drag, even though 'feedback' is nominally strong ($\mathcal{F} \gg 1$).

Fig. 4 also shows the evolution of the gas surface density τ_g. At times when the rates of gas sublimation and accretion evolve relatively slowly, the density profile is well described by a broken power-law distribution $\tau_g \propto x^{-n}$ (for $x < 1$) and $\tau_g \propto x^{-(n+1/2)}$ ($x > 1$) for $n = 3/2$. As shown in Appendix B, this profile is consistent with steady-state analytic solutions of the diffusion equation (equation 27 with $\Lambda = 0$) given a viscosity of the form $\nu \propto r^n$ ($n = 3/2$ for an isothermal α-disc model assumed here) and a constant source of mass at $x = 1$ (see equation B17). Solid–gas coupling thus also has little impact on the gas distribution in optically thin debris discs.

4.4 Optically thick ring

Although gas drag has no significant effect on the evolution of optically thin discs, it can be substantially more important for optically thick discs. Fig. 6 shows our calculation of the disc evolution in the case of an initially optically thick ring of dust ($\tau_{d,0} = 10$), again calculated for characteristic parameters $b_{PR} = 10^{-2}$, $\zeta_{in} = 0.04$, $x_0 = 5$ and $\Delta x = 0.5$, but now for only marginally strong feedback $\mathcal{F} = 2$. The top panel shows the full calculation including gas drag in the same format as Fig. 4, while for comparison the bottom panel shows for the same calculation with the drag artificially turned off. Fig. 7 shows the gas accretion rate on to the WD surface $\dot{M}_Z \equiv \dot{M}_g(x = 0)$ as a function of time for both cases.

First note from Fig. 6 that, in cases both with and without gas drag, the disc develops an extremely sharp profile near its outer edge. This sharp cut-off results from the exponential saturation of the accretion rates both due to PR drag $\dot{M}_{PR} \propto 1 - \exp[-\tau_d/\zeta]$ (equation 22) and due to aerodynamic drag $\dot{M}_a \propto 1 - \exp[-\tau_d]$ (equation 24), which are significantly more effective per unit mass in optically thin regions of the disc. Since the outer edge of the initial solid distribution is necessarily optically thin, this results in a pile-up of material at the location where the outer edge becomes moderately optically thick (BR11).

Figs 6 and 7 also illustrate the dramatic effect that gas drag has on the disc evolution. Again, in the cases both with and without drag, the distribution of solids initially develops an optically thin 'tail' ($\tau_d \ll 1$) at radii between the sublimation point $x = 1$ and the innermost location where the disc first becomes optically thick $x = x_{thick} \lesssim x_0$.

Without gas drag (Fig. 6b) the tail supplies an accretion rate from the optically thick disc to the sublimation radius which is approximately constant in time and radius. As shown in BR11, its value $\dot{M}_{PR}(x \approx x_{thick}; \tau_d \gtrsim 1) \approx \dot{M}_{PR,in}/x_0$ is set by the rate due to PR drag from the inner edge of the optically thick ring. The time-scale for the *entire* ring of dust to accrete through the tail is thus given by

$$t_{acc,thick} \simeq \frac{M_{tot}}{\dot{M}_{PR,in}/x_0} \approx \frac{x_0^3 \tau_{d,0}(\Delta x/x_0)}{b_{PR}\mathcal{F}} t_\nu \qquad \text{(no gas drag)}, \quad (49)$$

where M_{tot} is the total disc mass from equation (47) and we have used the definition of b_{PR} from equation (35). Substituting the relevant parameters for the above calculation ($x_0 = 5$, $b_{PR} = 10^{-2}$, $\tau_{d,0} = 10$ and $\Delta x = 0.5$) one finds a long accretion time-scale of $t_{thick} \approx 10^4\, t_\nu$ and a relatively low accretion rate of $\dot{M}_Z \approx 0.2\dot{M}_{PR,in}$, both consistent with the results of the 'without gas drag' case shown in the top panel of Fig. 7.

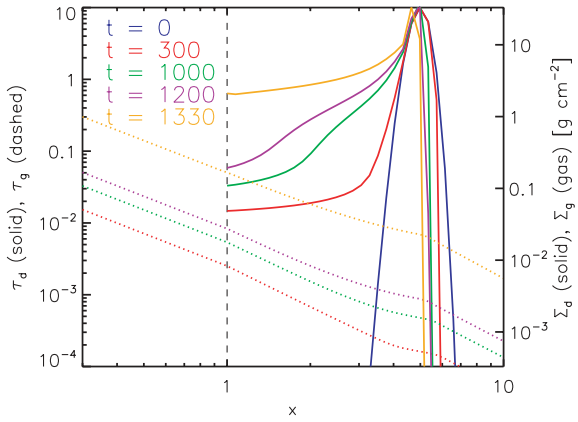

(a) With Gas Drag

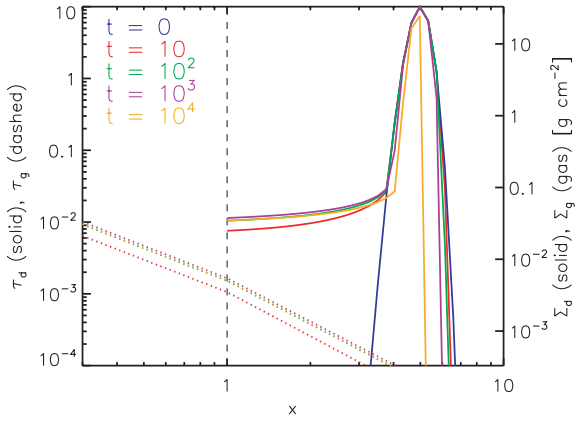

(b) Without Gas Drag

Figure 6. Similar to Fig. 4, but now calculated for an *optically thick* ring of dust with $\tau_{d,0} = 10$, $x_0 = 5$ and $\Delta x = 0.5$. Snapshots are shown at several times with different colours, in units of the viscous time at $x = 1$. The calculation is performed for parameters $b_{PR} = 10^{-2}$, $\zeta_{in} = 0.04$ and $\mathcal{F} = 2$. Panel (a) shows the calculation including aerodynamic drag between the gas and solids $\dot{M}_a$, while panel (b) shows the same calculation but with the drag artificially turned off.

With gas drag, however, the evolution of $\dot{M}_Z$ is dramatically altered (top panel). Instead of the accretion rate remaining approximately constant in time, Fig. 7 shows that $\dot{M}_Z$ initially increases exponentially on a time-scale of $t \approx 10^3 t_\nu$ (a 'build-up' stage), before 'running away' at a super-exponential rate. During this process, the entire solid disc is consumed on a time-scale which is a factor of $\sim$10 times shorter than in the case without gas drag, with the accretion rate during the final runaway reaching a peak value of $\sim 10^3$ times higher than the PR rate. As discussed in Section 1.1, such a runaway process was predicted by R11b, who showed that if feedback is strong ($\mathcal{F} \gtrsim 1$; $t_\nu \gtrsim t_s$) then the surface density of gas builds up near the sublimation radius $x \gtrsim 1$ due to drag-induced accretion faster than it can be reduced by viscous diffusion. Because the drag-induced accretion rate $\dot{M}_a$ is itself proportional to the gas surface density (equation 24), the build-up of mass at radii $x \gtrsim 1$ results in a runaway.

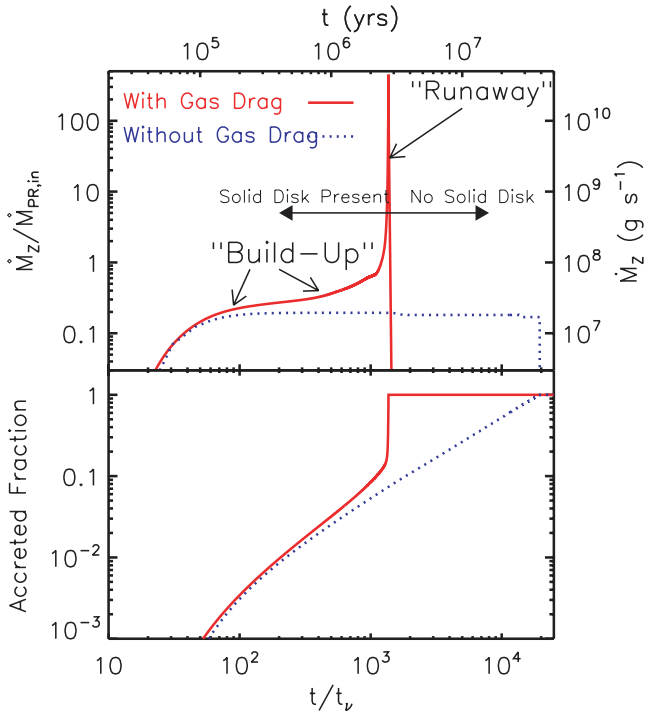

Figure 7. Top panel: gas accretion rate on to the WD surface $\dot{M}_Z$ in units of $\dot{M}_{\rm PR,in}$ as a function of time for the calculation shown in Fig. 6. Note that aerodynamic drag, starting at the inner edge of the optically thick part of the disc and moving inwards with time, causes an exponential 'build-up' and eventual 'runaway' in the accretion rate on a time-scale of $t \approx 10^3 t_\nu$. Bottom panel: fraction of the accreted mass for the calculation shown in the top panel. Note that most of the total mass is accreted during the final runaway phase. In plotting dimensional units we have adopted a fiducial WD debris disc model (Section 4.2).

Our results confirm that a runaway occurs, but the details of the process differ somewhat from those predicted by R11b. The simplified 'one-zone' model of R11b assumed that the solid disc at radii $x \gtrsim 1$ is at all times optically thick. When $\tau_{\rm d} \gg 1$, the rate of gas drag accretion $\dot{M}_a \propto 1-\exp(-\tau_{\rm d})$ (equation 24) saturates at the maximum value, such that runaway grows on the sublimation time-scale of $\approx t_{\rm s} = t_\nu/\mathcal{F}$ (equation 26). In our calculation, however, Fig. 7 shows that the runaway is delayed until a time-scale of $t \equiv t_{\rm run} \sim 10^3 t_\nu$ which is much longer than $t_{\rm s}$. As we now discuss, this delay occurs because the solids at radii $x \gtrsim 1$ are initially part of the *optically thin* tail created by PR drag, which couples relatively weakly to the gas.

Although gas drag is weak just outside the sublimation radius where $\tau_{\rm d} \ll 1$, the gas distribution extends to radii $x \gg 1$ due to viscous spreading (see equation 51), where it overlaps with the optically thick solid disc. Fig. 6 shows that the drag force between this gas tail and solids at the inner edge of the optically thick disc $x \approx x_{\rm thick}$ creates an 'enhancement' in the solid profile with $\tau_{\rm d} \sim 1$. The 'build-up' stage occurs as this enhancement moves inwards with time. Finally, once the enhancement reaches the sublimation radius, the condition $\tau_{\rm d}(r \sim R_{\rm s}) \approx 1$ is satisfied and the full runaway occurs in much the same way as predicted by R11b, albeit after a much longer delay time $t_{\rm run} \gg t_{\rm s}$.

The delay until runaway $t_{\rm run}$ can be estimated as the time required for the mass associated with $\tau_{\rm d} \approx 1$ to propagate from $x \approx x_{\rm thick} \lesssim x_0$ to $x = 1$ at the rate set by gas drag accretion $\dot{M}_a$:

$$t_{\rm run} \simeq \frac{\pi x_{\rm thick}^2 \Sigma_0}{\dot{M}_a(x \approx x_{\rm thick};\, \tau_{\rm d} \approx 1)} \approx \frac{x_{\rm thick}^3}{b_{\rm PR}\mathcal{F}^2} t_\nu, \tag{50}$$

where we have used the definitions of $A_{\rm in}$, $\mathcal{F}$ and $b_{\rm PR}$ from equations (25), (34) and (35), respectively. We calculate $\dot{M}_a(x \approx x_{\rm thick})$ (equation 24) using the analytic expression for the gas surface density

$$\Sigma_{\rm g}(r) = \frac{\dot{M}_{\rm d}(x=1)t_\nu}{3\pi r^2} \tag{51}$$

derived in Appendix B (equation B17) assuming $\nu \propto r^n$ for $n = 1$ (equation 30) and approximating the sublimation rate by its initial PR-driven value $\dot{M}_{\rm d}(x=1) \simeq \dot{M}_{\rm PR,in}/x_0$. We also adopt $\eta = 7/4$ appropriate for $\tau_{\rm g} \propto r^{-2}$ (equation 5).

In order to verify that the above explanation is self-consistent, one must check that the accretion rate due to aerodynamic drag indeed exceeds that due to PR drag at the inner edge of the optically thick disc. Their ratio is given by

$$\left.\frac{\dot{M}_a}{\dot{M}_{\rm PR}}\right|_{x\approx x_{\rm thick};\tau_{\rm d}\approx 1} \approx \frac{49}{48}\mathcal{F}, \tag{52}$$

where we have again assumed $\eta = 7/4$ and made use of equations (24), (25) and (34) for $\dot{M}_a$, $A_{\rm in}$ and $\mathcal{F}$, respectively. Equation (52) confirms that aerodynamic drag is at least comparable to PR drag for $\mathcal{F} > 1$, thus demonstrating that the conditions necessary to 'trigger' a runaway are satisfied rather generically (see also Appendix C). Also note that the fact that $t_{\rm run}$ rapidly increases with $x_{\rm thick}$ confirms our implicit assumption that the runaway time-scale is dominated by the earliest times when $x_{\rm thick}$ is largest.

For parameters relevant to the above calculation ($b_{\rm PR} = 10^{-2}$, $\mathcal{F} = 2$ and $x_0 = 5$), equation (50) predicts a runaway time-scale of $t_{\rm run} \sim 10^3 t_\nu$, consistent with the results shown in Fig. 6 to within a factor of $\approx$2.

The bottom panel of Fig. 7 shows the fraction of accreted mass as a function of time for the same calculation. Note that only $\sim$10 per cent of the total disc mass is accreted during the build-up stage, with the majority instead consumed during the final runaway. The maximum accretion rate achieved during runaway can be estimated by assuming that the entire solid disc mass $M_{\rm tot}$ (equation 47) is consumed on the viscous time t_ν (equation 2):

$$\dot{M}_{\rm max} \approx \frac{M_{\rm tot}}{t_{\rm visc}} \approx \frac{\tau_{\rm d,0} x_0^2 (\Delta x/x_0)}{b_{\rm PR}\mathcal{F}} \dot{M}_{\rm PR,in}. \tag{53}$$

Unlike in cases without gas feedback, for which the accretion rate is limited to the maximum rate set by PR drag $\dot{M}_{\rm PR,in}$, note that $\dot{M}_{\rm max}$ is proportional to the total disc mass $M_{\rm tot} \propto \tau_{\rm d,0}$ and hence can substantially exceed $\dot{M}_{\rm PR,in}$. Also note, however, that equation (53) applies only to systems well above the runaway threshold ($\mathcal{F} \gg 1$; see below), for which $t_{\rm run} \ll t_{\rm acc,thick}$ (without gas coupling; equation 49), such that most of the total mass is indeed accreted during the final runaway.

Fig. 8 shows $\dot{M}_Z(t)$, calculated for several models using the same parameters as in Figs 6 and 7 ($x_0 = 5$, $b_{\rm PR} = 0.01$ and $\tau_{\rm d,0} = 10$) but for different values of the feedback parameter $\mathcal{F}$. Note that runaway occurs only for $\mathcal{F} \gtrsim 1$, remarkably similar to the threshold predicted by R11b. Also note that the delay time-scale to runaway scales $t_{\rm run} \propto \mathcal{F}^{-2}$, consistent with the analytic prediction in equation (50). The rise time of the accretion rate from zero to the PR value during the initial build-up phase also varies with the parameters $b_{\rm PR}$ and $\mathcal{F}$, as determined instead in this case by the optically thin accretion time $t_{\rm acc,thin} \propto \mathcal{F}^{-1} b_{\rm PR}^{-1}$ (equation 48).

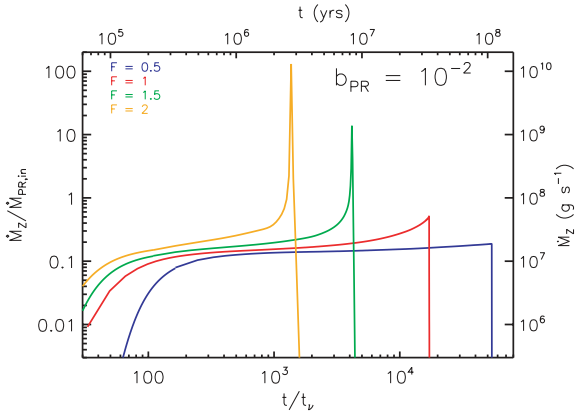

Figure 8. Gas accretion rate on to the WD surface $\dot{M}_Z \equiv \dot{M}(x = 0)$ (in units of $\dot{M}_{\rm PR,in}$) as a function of time, calculated for several solutions with the same parameters as in Figs 6 and 7 ($x_0 = 5$, $b_{\rm PR} = 0.01$ and $\tau_{\rm d,0} = 10$) but for different values of the feedback parameter $\mathcal{F} = 0.5$ (blue), 1 (red), 1.5 (green) and 2 (orange). Note that the condition $\mathcal{F} \gtrsim 1$ describes well the threshold for a runaway, while the delay time until runaway scales as $t_{\rm run} \propto \mathcal{F}^{-2}$ (equation 50). In plotting dimensional units, we have adopted a fiducial WD debris disc model (Section 4.2).

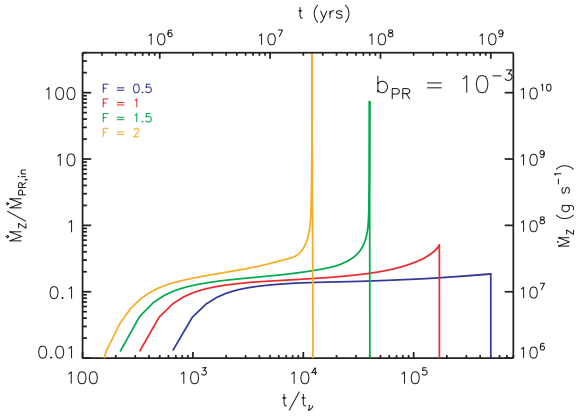

Figure 9. Same as Fig. 8, but calculated for $b_{\rm PR} = 10^{-3}$. Note that again the threshold condition for runaway is well described as $\mathcal{F} \gtrsim 1$, but that the delay time until runaway $t_{\rm run} \propto b_{\rm PR}^{-1}$ occurs later (at fixed $\mathcal{F}$) due to the lower value of $b_{\rm PR}$ (equation 50).

Figs 9 and 10 show similar results, but now calculated assuming lower values for the PR parameter $b_{\rm PR} = 10^{-3}$ and 10^{-4}, respectively. In both cases, we again find that $\mathcal{F} \gtrsim 1$ is a good estimate of the threshold for runaway, and we confirm that $t_{\rm run} \propto b_{\rm PR}^{-1}\mathcal{F}^{-2}$, as predicted by equation (50).

A final important feature of our results is the sensitive dependence of the runaway time-scale on the innermost radius where the disc becomes optically thick $t_{\rm run} \propto x_{\rm thick}^3$ (equation 50). Fig. 11 shows our results for $\dot{M}_Z(t)$ from a series of calculations identical to those shown in Fig. 8, except calculated for an initial Gaussian ring centred at a smaller radius $x_0 = 2 \approx x_{\rm thick}$. The evolution of $\dot{M}_Z$ is qualitatively similar to that shown in Fig. 8 for a ring centred at $x_0 = 5$, except that the runaway time occurs an order of magnitude sooner, consistent with the ratio $\approx (2/5)^3$ predicted by equation (50).

Fig. 6(a) also shows that when gas drag is important, the radial profile of $\Sigma_{\rm g}$ does not follow a single power law for $r > R_{\rm in}$, as it does without gas drag, see Figs 4 and 6(b). Instead, $\Sigma_{\rm g}$ decays slower with r at distances where there is an overlap between gas and the optically thick segment of the disc of solids. This is understood

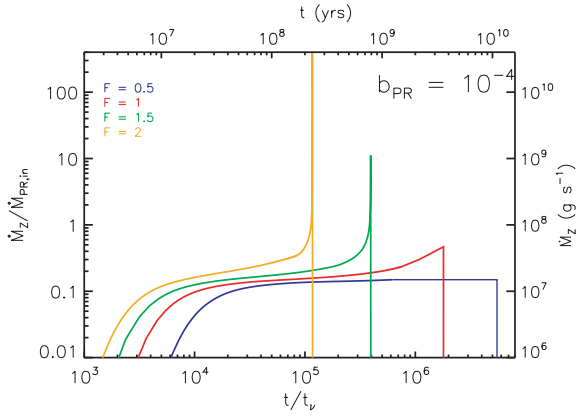

Figure 10. Same as Figs 8 and 9, but calculated for $b_{\rm PR} = 10^{-4}$.

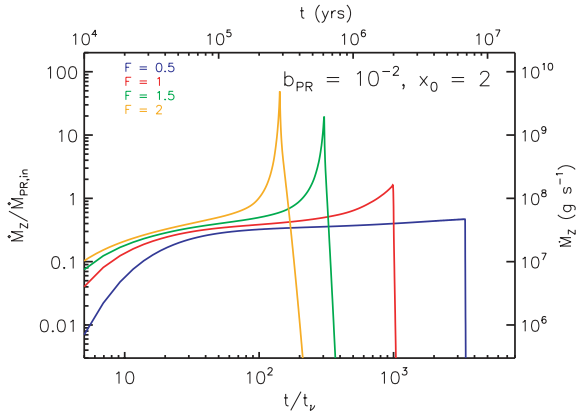

Figure 11. Same as Fig. 8 but calculated for an initial Gaussian ring with a smaller central radius $x_0 = 2$. Note that again the runaway threshold occurs at $\mathcal{F} \approx 1$, but that the delay time until runaway $t_{\rm run} \propto x_0^3$ at fixed $\mathcal{F}$ occurs much earlier (equation 50).

to be a direct consequence of the back-reaction of the aerodynamic drag on the gaseous disc, i.e. the non-trivial Λ in equation (27).

4.5 Optically thick top-hat

Our calculations have thus far focused on the idealized case of a Gaussian ring for the initial dust radial profile (equation 46). However, the same qualitative results, including the runaway process, are of general applicability. To illustrate this point, in Figs 12 and 13 we show the gas/dust evolution and gas accretion rate for a calculation which assumes that the initial distribution of solids instead has a 'top-hat' profile, characterized by a constant value of $\tau_{\rm d} = 1$ from $x = 2$ to 6. We again assume characteristic values for the parameters $\mathcal{F} = 2$, $b_{\rm PR} = 10^{-2}$ and $\zeta_{\rm in} = 0.04$. Though still highly idealized, a top-hat distribution of solids spread over a factor of a few in radii is probably a more accurate description of the initial distribution of solids following the tidal disruption of a minor body.

Fig. 12 shows that the disc evolves in a qualitatively similar fashion to the Gaussian ring shown in Figs 6 and 7. In particular, an optically thin tail develops initially, which later increases due to gas drag, before a runaway occurs at $t = t_{\rm run} \approx 200\, t_\nu$ once solids with $\tau_{\rm d} \approx 1$ reach the sublimation radius. The time-scale until runaway can again be reasonably well estimated using the analytic estimate in equation (50), provided that one replaces the inner radius of the optically thick ring $x_{\rm thick}$ with the inner radius $x = 2$ of the initial optically thick top-hat distribution.

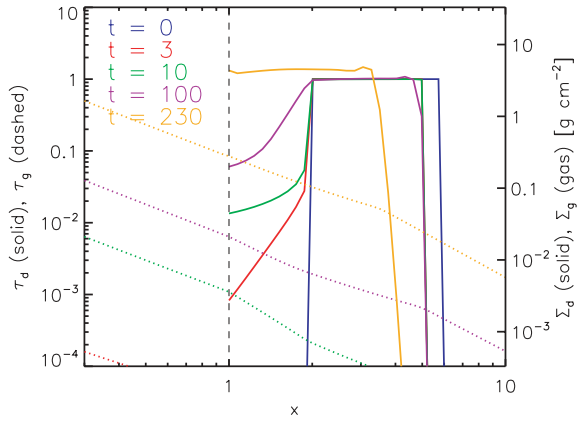

Figure 12. Similar to Figs 6, but now calculated assuming a flat 'top-hat' profile between $x = 2$ and 6 for the initial distribution of optically thick dust. The dust (solid lines) and gas (dotted lines) density profiles are shown at several times $t = 0$ (blue), $t = 3$ (red), $t = 10$ (green), $t = 100$ (purple) and $t = 230$ (orange), in units of the viscous time at $x = 1$. The calculation is performed for parameters $b_{\rm PR} = 10^{-2}$, $\zeta_{\rm in} = 0.04$ and $\mathcal{F} = 2$.

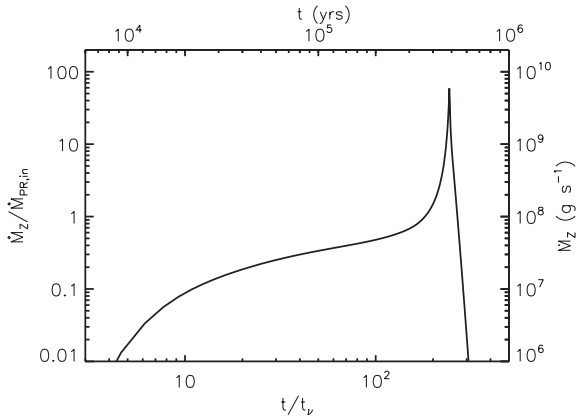

Figure 13. Gas accretion rate on to the WD surface $\dot{M}_Z$ for the top-hat calculation shown in Fig. 12. Note that the accretion evolution is similar to the case of a Gaussian ring with a similar characteristic inner radius (see the $\mathcal{F} = 2$ case in Fig. 11).

We conclude that the runaway accretion of solids due to gas drag is an inevitable fate for optically thick discs in the presence of strong feedback $\mathcal{F} \gtrsim 1$. With everything else fixed, the time-scale for runaway depends on the minimum radius of the optically thick material $x_{\rm thick}$ (equation 50), while the maximum accretion rate depends on the mass of the solid disc (equation 53).

5 APPLICATIONS AND OBSERVATIONAL TESTS

In this section we present applications of our calculations and observational implications of the runaway accretion model.

5.1 True versus 'measured' accretion rate

Because the time-scale required for heavy elements to diffuse below the outer convective zone of the WD is much shorter than the WD age, metals observed at the surface indicate recent pollution by an external source, such as accretion from a gaseous disc. Under the joint action of accretion and gravitational settling, the total mass of metals in the convective zone M_{Z_i} with charge Z_i evolves according to (e.g. Koester & Wilken 2006)

$$\frac{{\rm d}M_{Z_i}}{{\rm d}t} = \dot{M}_{Z_i} - \frac{M_{Z_i}}{t_{{\rm set},i}}, \tag{54}$$

where $\dot{M}_{Z_i} = \dot{M}_Z X_{Z_i}$, X_{Z_i} is the mass fraction of metal Z_i in the accreting gas, and $t_{{\rm set},i}$ is the settling (or diffusion) time of element Z_i, which depends on the temperature and composition of the WD (e.g. Paquette et al. 1986). A typical WD of mass $M_{\rm WD} = 0.6\,{\rm M}_\odot$, for instance, requires $\sim 2 \times 10^8$ yr and 6×10^8 yr to cool to a temperature of $T \simeq 1.5 \times 10^4$ K and $T \simeq 1.0 \times 10^4$ K, respectively (Bergeron, Saumon & Wesemael 1995). In a H-rich atmosphere (DAZ WDs), over this time interval the settling times of most observed elements increase from $t_{{\rm set},i} \sim$ days to $\sim 10^3$ years. For a He-rich atmosphere (DBZ WD), in contrast, the convective zone is much larger, resulting in a much longer settling time $t_{{\rm set},i} \approx 10^{5.5}$–$10^6$ yr, which depends less sensitively on temperature (Paquette et al. 1986).

Gas is fed from the sublimation radius to the WD surface on the viscous time t_ν (equation 2). If $t_{{\rm set},i} \ll t_\nu$, then the atmospheric composition reaches a steady state ${\rm d}M_{Z_i}/{\rm d}t = 0$, in which the mass in the convective zone is approximately given by $M_{Z_i} \approx \dot{M}_{Z_i} t_{{\rm set},i}$. Since the surface composition M_{Z_i} is measured via spectral line diagnostics and theoretical models of the total mass in the WD convective zone, and $t_{{\rm set},i}$ is also calculable from the known properties of the WD, then the total instantaneous gas accretion rate in this limit is well estimated by the expression (e.g. Koester & Wilken 2006; Farihi et al. 2009)

$$\dot{M}_Z \simeq \frac{M_{Z_i}}{X_{Z_i} t_{{\rm set},i}} \equiv \dot{M}_{Z,{\rm obs}} \quad (t_{{\rm set},i} \ll t_\nu). \tag{55}$$

Equation (55) provides a reliable estimate of $\dot{M}_Z$ in the case of hot DAZ WDs (which easily satisfy $t_{{\rm set},i} \ll t_\nu$), but it can be grossly inaccurate in the opposite limit that $t_{{\rm set},i} \gtrsim t_\nu$, as may apply to DBZ or cool DAZ WDs.

Fig. 14 illustrates this point in the context of our models by showing a comparison of the actual gas accretion rate $\dot{M}_Z$ from our fiducial solution from Fig. 6 to the 'measured' value $\dot{M}_{Z,{\rm obs}}$ one obtains by naively applying equation (55), the latter shown for different assumptions about the ratio $t_{{\rm set},i}/t_\nu = 10$, 10^2 and 10^3. We

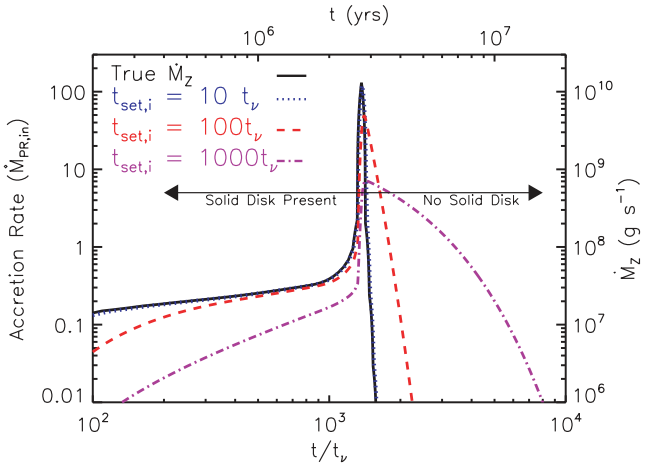

Figure 14. Actual gas accretion rate $\dot{M}_Z$ from our fiducial solution shown in Figs 6(a) and 7 (solid line) compared to the 'measured' accretion rate $\dot{M}_{{\rm obs},Z}$ calculated using the steady-state approximation (equation 55), shown for different assumptions about the value of $t_{\rm diff} = 10\ t_\nu$ (blue dotted line), $10^2\ t_\nu$ (red dashed line) and $10^3 t_\nu$ (green dot–dashed line), where t_ν is the accretion time-scale at the sublimation radius. See text for details.

calculate $M_Z(t)$ by integrating equation (54) directly, assuming that $X_{Z,i} = 1$ and using $\dot{M}_{Z,i}$ derived from our calculations shown in Fig. 7.

In the case that $t_{\rm set,i} \lesssim 10t_\nu$, Fig. 14 shows that 'measured' accretion rate $\dot{M}_{Z,\rm obs}$ indeed accurately reflects the true instantaneous accretion rate. On the other hand, when $t_{\rm set,i} \gg 10t_\nu$, $\dot{M}_Z$ and $\dot{M}_{Z,\rm obs}$ may differ substantially. In particular, prior to the time when $\dot{M}_Z$ peaks, $\dot{M}_{Z,\rm obs}$ *underestimates* the true accretion rate by a factor of up to ∼10. Since this epoch corresponds to when the solid disc is still present, our results suggest that one should exercise caution when interpreting the accretion rates in those systems with an observed IR excess when $t_{\rm set,i} \gg t_\nu$. On the other hand, at times after $\dot{M}_Z$ peaks, $\dot{M}_{Z,\rm obs}$ instead *overestimates* the true accretion rate. This discrepancy is one explanation for those systems shown in Fig. 1 with high measured accretion rates $\dot{M}_{Z,\rm obs}$, yet no IR excess indicating the current presence of a solid disc.

One concrete application of the results in Fig. 14 is to cool DBZ WDs with large $t_{\rm set,i}$, for which one predicts that $\dot{M}_{Z,\rm obs}$ underestimates the true current accretion rate $\dot{M}_Z$ for systems with detected near-IR excesses (indicating a current solid disc), whereas $\dot{M}_{Z,\rm obs}$ instead overestimates $\dot{M}_Z$ in DBZ WD systems without solid discs. Note also that since the *ratio* of the inferred accretion rates of different elements is subject to similar uncertainties, one should also exercise caution when using similar methods to infer the precise composition of the accreted bodies in systems for which $t_{\rm set,i} \gtrsim t_\nu$ (cf. Xu & Jura 2012). Previous works have attempted to generalize estimates of $\dot{M}_Z$ to cases when $t_{\rm set,i} > t_\nu$ (or to constrain the entire accretion history of the event), by adopting simplified assumptions about the time evolution of the accretion rate (e.g. Jura et al. 2009a), e.g. $\dot{M} \propto \exp[-t/t_{\rm acc}]$, where $t_{\rm acc}$ is the accretion timescale. However, given the complicated accretion evolution in cases when feedback is effective, we again urge caution when adopting such simplified models.

We conclude with one final point regarding what inferences can be drawn about the past accretion history of a WD using the currently 'measured' accretion rate $\dot{M}_{Z_i,\rm obs} \equiv X_{Z_i}\dot{M}_{Z,\rm obs}$ given by equation (55). Equation (54) can be trivially integrated to give the mass of metals with charge Z_i in the WD atmosphere as a function of time, provided that the evolution of the true accretion rate $\dot{M}_{Z_i}(t)$ is known:

$$M_{Z_i}(t) = \int_0^t \dot{M}_{Z_i}(t')\mathrm{e}^{-(t-t')/t_{\rm set,i}}\,\mathrm{d}t', \tag{56}$$

where we have assumed that $M_{Z_i} = 0$ at time $t = 0$. If we define $\dot{M}_{Z_i,\rm max}(< t)$ to be the maximum value reached by the true accretion rate $\dot{M}_{Z_i}$ in the past, then one estimates that

$$\begin{aligned} M_{Z_i}(t) &< \dot{M}_{Z_i,\rm max}(< t)\int_0^t \mathrm{e}^{-(t-t')/t_{\rm set,i}}\,\mathrm{d}t' \\ &= \dot{M}_{Z_i,\rm max}(< t)t_{\rm set,i}\left(1-\mathrm{e}^{-t/t_{\rm set,i}}\right), \end{aligned} \tag{57}$$

such that for any t one has

$$\dot{M}_{Z_i,\rm obs}(t) = \frac{M_{Z_i}(t)}{t_{\rm set,i}} < \dot{M}_{Z_i,\rm max}(< t). \tag{58}$$

Thus, the currently 'measured' value of $\dot{M}_{Z_i,\rm obs}$ always provides a *lower limit* on the maximum $\dot{M}_{Z_i}$ achieved in the past. Conversely, for any given 'measured' value of $\dot{M}_{Z_i,\rm obs}$, one can deduce that during some epoch in the past the *true* mass accretion rate $\dot{M}_{Z_i}$ was *at least as high* as $\dot{M}_{Z_i,\rm obs}$.

5.2 Accretion rate distribution

Given a complete model for the evolution of WD debris discs, one can begin to address observational questions, such as the probability of detecting a WD debris disc system when the accretion rate has some particular value. Figs 15–17 show several such examples of the normalized distribution $\mathrm{d}N_y/\mathrm{d}(\log y)$ of observed accretion rates $y = \dot{M}_Z/\dot{M}_{\rm PR,in}$. Each distribution is created using a single disc evolution calculation from Section 4, under the highly idealized assumptions that (1) all WD debris discs are identical to the model from which each distribution was created and (2) the system is equally likely to be detected at any moment during active gas

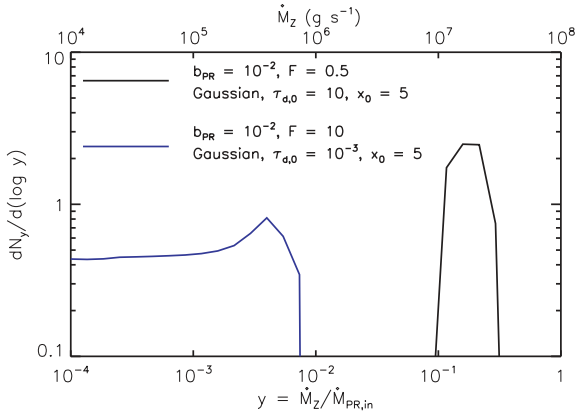

Figure 15. Probability distribution $\mathrm{d}N_y/\mathrm{d}(\log y)$ for detecting a WD debris disc when the accretion rate is $y = \dot{M}_Z/\dot{M}_{\rm PR,in}$, calculated for two solutions *without* runaway accretion. A blue line shows the distribution calculated for the optically thin disc with $\tau_{\rm d,0} = 10^{-3}$ from Figs 4 and 5. A black line shows the distribution calculated for the optically thick disc ($\tau_{\rm d,0} = 10$) with a feedback parameter $\mathcal{F} = 0.5$ too low for runaway accretion. In both cases, the accretion rate peaks below the characteristic value set by PR drag, which is insufficient to explain the highest measured WD accretion rates shown in Fig. 1. In plotting dimensional units, we have adopted a fiducial WD debris disc model (Section 4.2).

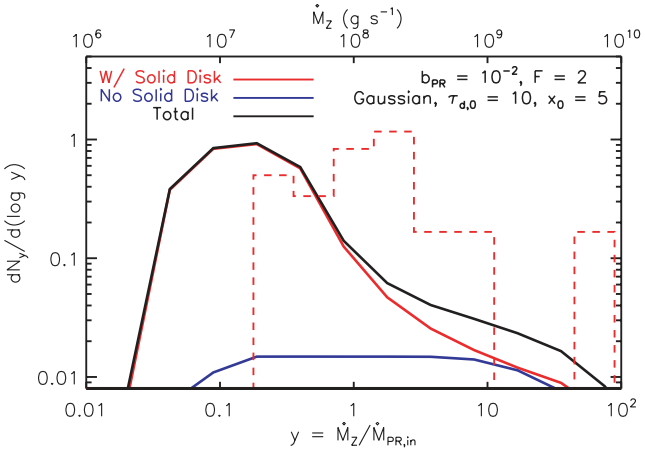

Figure 16. Probability distribution $\mathrm{d}N_y/\mathrm{d}(\log y)$ for detecting a WD debris disc when the accretion rate is $y = \dot{M}_Z/\dot{M}_{\rm PR,in}$, calculated for the evolution of the optically thick Gaussian ring ($\tau_{\rm d,0} = 10$, $x_0 = 5$ and $\Delta x = 0.5$) with runaway accretion ($\mathcal{F} = 2$) shown in Figs 6 and 7. Note that the runaway process results in a wider distribution, extending to much higher accretion rates than in the otherwise identical calculation without runaway accretion ($\mathcal{F} = 0.5$) shown in Fig. 15. Note that the dimensional units shown on the top axis apply only to the theoretical curves (assuming our fiducial WD debris disc model in Section 4.2).

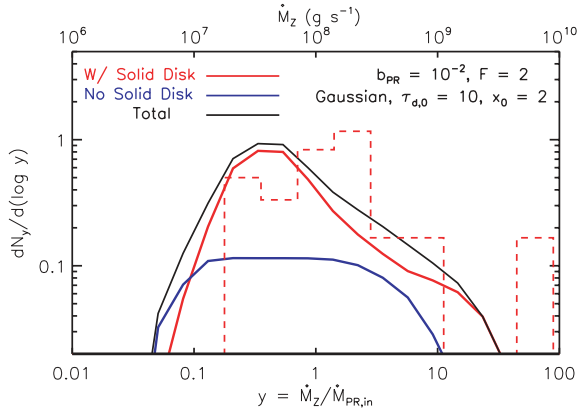

Figure 17. Same as Fig. 16, but calculated using the Gaussian ring centred at the smaller central radius $x_0 = 2$ (Fig. 11).

accretion. Although neither of these assumptions is likely valid, these distributions nevertheless inform what kinds of debris disc systems could contribute to the observed distribution of accretion rates shown in Fig. 1.

Fig. 15 shows the distribution calculated for two cases *without* runaway accretion: the optically thin ($\tau_{d,0} = 10^{-3}$) Gaussian ring shown in Figs 4 and 5 (blue line), and the optically thick ($\tau_{d,0} = 10$) Gaussian ring without strong feedback ($\mathcal{F} = 0.5$) shown in Figs 6 and 7 (black line). In both cases, the distribution is fairly narrowly concentrated about the characteristic accretion rate set by PR drag acting alone. Accretion rates $\dot{M}_Z \lesssim \dot{M}_{PR,in}$ at the low end of the measured values in Fig. 1 are thus consistent with those resulting from a superposition of such systems, as may result e.g. from a range in the masses or orbital parameters of disrupted asteroids. However, disc evolution without runaway accretion cannot explain the highest observed accretion rates $\dot{M}_Z \sim 10{-}100\dot{M}_{PR,in}$.

Figs 16–18 show the accretion rate distribution (solid black line) for several disc evolutions *with* runaway accretion. In these cases we further divide the distribution between those times when the solid disc is still present (solid red line) and those times after it has completely sublimated (solid blue line). Also plotted for comparison with a dashed red line is the normalized distribution of measured WD metal accretion rates shown in Fig. 1 from the sample of Farihi et al. (2009, 2010b), including only systems with an IR excess. Note that our results correspond to the true accretion rate $\dot{M}_Z$, while the observational sample uses the 'measured' rates $\dot{M}_{Z,obs}$ (see

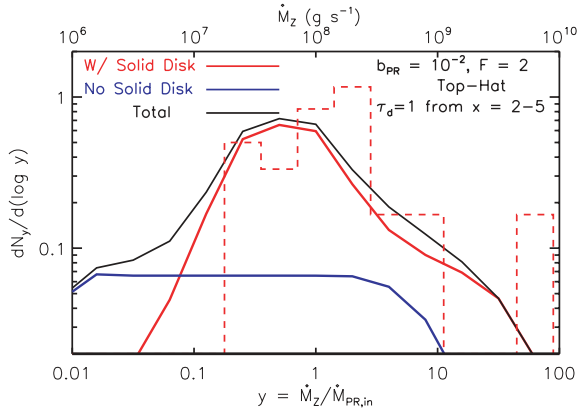

Figure 18. Same as Fig. 16 but calculated using the solution for the 'top-hat' initial density profile (Figs 12 and 13).

Section 5.1). Thus, one should exercise caution when comparing them.

Fig. 16 shows the fiducial case of an optically thick Gaussian disc ($\tau_{d,0} = 10$, $x_0 = 5$; $\mathcal{F} = 2$; $b_{PR} = 10^{-2}$), as shown in Figs 6(a) and 7. The probability distribution in this case still peaks at a relatively low accretion rate of $\dot{M}_Z \sim 0.1{-}1\dot{M}_{PR,in}$ set by the characteristic range in accretion rate during the 'build-up' to runaway. However, the final stages in the runaway process produce a substantial 'tail' in the distribution extending to much higher accretion rates $\dot{M}_Z \sim 10{-}100\dot{M}_{PR,in}$.

Although small number statistics and potential selection effects introduce many uncertainties, note the overall qualitative similarity between the shapes of the theoretical and observed accretion rate distributions. A somewhat better agreement with the observed distribution is obtained for discs formed with more compact inner radii, as shown in Figs 17 and 18 for the cases of a Gaussian ring centred at $x_0 = 2$ (Fig. 7) and the top-hat distribution with $\tau_d = 1$ from $x = 2$ to 5 (Fig. 13), respectively. The top-hat distribution in particular illustrates the broad accretion rate distribution produced by even an ensemble of identical systems in the (most physically realistic) case of a radially extended disc that undergoes runaway accretion.

Figs 16–18 also illustrate that the probability of detecting actively accreting systems when the solid disc is still present (solid red line) is much greater than after the solid disc has entirely sublimated (solid blue line). We caution, however, against attaching much significance to a direct comparison between our predictions for the fraction of actively accreting systems without solid discs and the fraction of metal-rich WDs with no detected IR excess, given potential selection effects and other ways that IR emission could be difficult to detect even in systems with discs (see Fig. 15 and Section 6).

6 DISCUSSION

Our results demonstrate that runaway accretion is a ubiquitous feature in the evolution of WD debris discs with strong gas–solid coupling and/or weak gas viscosity. We find that the condition $\mathcal{F} \equiv t_\nu/t_s \gtrsim 1$ for the runaway predicted by R11b using local calculations is a surprisingly accurate diagnostic of the runaway threshold.

In Appendix C, we present and analyse a simple global analytical model of the coupled evolution of the two discs which makes two simplifying assumptions: (a) that the back-reaction of aerodynamic drag on the gaseous disc can be neglected and (b) that the disc of solids is always optically thick at R_{in}. Even though this model is fully global and far more realistic compared to the calculations done in R11b, we are still able to derive from it analytically the runaway condition (equation C8), which is essentially analogous to $\mathcal{F} \gtrsim 1$. This additionally reaffirms the robustness of the runaway threshold found in R11b and this work.

Is $\mathcal{F} > 1$ physically realizable in WD debris disc systems? If one adopts our standard model for the aerodynamic drag between solid and gaseous discs described in Section 2.1, then satisfying this condition $\mathcal{F} \gtrsim 1$ requires gas viscosity $\alpha_{in} \lesssim 10^{-2}{-}10^{-4}$ near the inner edge of the disc (see equation 44 and surrounding discussion). At first glance this condition appears unlikely to be satisfied because the gas temperature is sufficiently high $T_g \gg 10^3$ K that thermal ionization should be efficient, whereas observations of fully ionized accretion discs (King, Pringle & Livio 2007) and numerical simulations of the magneto-rotational instability (MRI)

in ideal MHD (e.g. Fromang & Papaloizou 2007; Davis et al. 2010) typically suggest higher values of $\alpha \sim 0.01$–0.1.

Note, however, that gas and solids overlap at the radii $\gtrsim R_{\rm s}$ in our model and *Spitzer* observations reveal that micron-sized dust grains are present in many systems (Jura et al. 2009b). The presence of small dust in the disc can significantly lower the ionization fraction below the nominal equilibrium value because small grains are very efficient at absorbing charge. Even though the observationally inferred mass of micron-sized Si grains ($\lesssim 10^{18}$ g; Jura et al. 2009b) is much less than that of a sizeable asteroid thought to give rise to a solid disc, small grains may still dominate the total surface area of particles. A lower free charge density increases the resistivity of the gas, which in turn reduces the effective turbulent viscosity by suppressing the MRI due to non-ideal MHD effects (e.g. Fleming, Stone & Hawley 2000). The relevant value of $\alpha_{\rm in}$ in our model could thus be much lower than would be expected in a fully ionized disc, thus making strong feedback $\mathcal{F} \gg 1$ much more likely.

In addition to lowering the viscosity, the runaway condition $\mathcal{F} \gg 1$ could also be satisfied if the interaction between gas and solids is stronger than is assumed in our baseline model in Section 2.1. Below we describe two such additional mechanisms for the solid–gas coupling: enhanced aerodynamic drag due to an eccentric gaseous disc (Section 6.1) and 'inductive coupling' by a magnetic field threading the disc (Section 6.2). Accounting for these additional possibilities, it appears quite possible that the conditions for runaway accretion are actually achieved in nature.

Our model provides useful predictions for the properties of gaseous discs fed by sublimation which may be verified by observations. In particular, equation (7) suggests a characteristic estimate of the gas surface density at $R_{\rm in}$ for $\dot{M}_Z \sim \dot{M}_{\rm PR}$. The value of $\Sigma_{\rm g}$ at this location can easily be higher than 10^{-2} g cm^{-2} if $\dot{M}_Z$ exceeds $\dot{M}_{\rm PR}$, as should be the case during runaway (but note that it is the true rate $\dot{M}_Z$ that sets $\Sigma_{\rm g}$, see Section 5.1 for details). We also point out that viscous evolution in our model naturally results in the profile of $\Sigma_{\rm g}(r)$, which is shallower for $r < R_{\rm in}$ than for $r > R_{\rm in}$, see equation (B17) and Fig. 2. This implies that the gas mass inside the cavity of the disc of solids is lower than one would naively assume, which might help explain the observed lack of line emission from this region of the gaseous disc (Melis et al. 2010).

The lifetime of discs that undergo runaway accretion is set predominantly by the delay time-scale until runaway $t_{\rm run}$ given in equation (50). Substituting the values of t_ν (equation 2) and $b_{\rm PR}$ (equation 35) into this expression, one finds that

$$t_{\rm life} \sim t_{\rm run} \simeq 5 \times 10^5 \mathcal{F}^{-1} \left(\frac{x_{\rm thick}}{2}\right)^3 \left(\frac{a}{\rm cm}\right) \ {\rm yr}, \qquad (\mathcal{F} > 1), \quad (59)$$

where we have adopted characteristic values for the gas temperature $T_{\rm g} = 5 \times 10^3$ K, solid particle density $\rho_{\rm d} = 2.5$ g cm^{-3} and mean molecular weight $\mu = 28 m_{\rm p}$. We normalize the inner edge of the optically thick disc to a characteristic value of $x_{\rm thick} \approx 2$, which best reproduces the observed WD accretion rate distribution (Fig. 17). Note that $t_{\rm life}$ is independent[3] of the (uncertain) strength of the disc viscosity $\alpha_{\rm in}$ and the precise form of the drag force between the solids and gas (except implicitly through the value of $\mathcal{F}$).

The lifetimes of the WD debris disc are poorly constrained by observations, but one can set a rough upper limit of $t_{\rm life} \lesssim 10^5$–$10^6$ yr (Kilic et al. 2008; Farihi et al. 2009; Girven et al. 2012). Equation (59) shows that this constraint translates into an upper limit on the characteristic particle size $a \lesssim (0.2$–$2)\mathcal{F}$ cm. For $\mathcal{F} > 1$ (as required for runaway to occur in the first place), one thus requires particles with a typical size $a \lesssim$ several cm, consistent with (relatively weak) existing observational constraints (e.g. Graham et al. 1990; Jura et al. 2007b).

An important outstanding question is why some WDs with high inferred accretion rates have no detected IR excess. Our calculations in Section 5.2 predict that the total fraction of actively accreting systems without solid discs should be relatively small, typically $\lesssim$20 per cent. As discussed in Section 5.1, one possible explanation in the case of systems with long metal diffusion times $t_{{\rm set},i} \gg t_\nu$ (as characterize WDs with cool temperatures and/or He-enriched atmospheres) is the discrepancy between the true instantaneous WD accretion rate and the value inferred using atmospheric abundances and the steady-state approximation. Fig. 14 shows that for $t_{{\rm set},i} \gtrsim 10^2$–$10^3 t_\nu$, the accretion rate inferred using the steady-state model can remain at a high level for a time-scale comparable to or longer than the disc lifetime itself even after the solid disc has completely sublimated.

Another possible explanation for high-$\dot{M}_Z$ systems without an IR excess is that a solid disc is in fact present but cannot be detected, for instance because of a poor viewing angle and/or because the disc is concentrated in a narrow ring of width $\Delta r \approx 0.01$–$1\,{\rm R}_\odot$ (Farihi et al. 2010b). Our calculations in Figs 6 and 12 confirm that this is a viable possibility by showing that optically thick discs largely maintain their original width, until the end of the disc lifetime when the runaway process is nearly complete.

We conclude by addressing several extensions to our standard model and outstanding issues to be explored further in future work.

6.1 Effects of non-circular gas motion

Our calculation of aerodynamic drag in Section 2.1 explicitly assumed that both the solid and gaseous materials move on purely *circular* orbits, in which case the difference in azimuthal velocity between the discs $v_{\phi,{\rm rel}}$ is due solely to the pressure support in the gaseous disc (equation 4). Since this velocity difference is relatively small (compared to, say, the orbital velocity), then the resultant aerodynamic coupling between the discs is not very strong. For this reason, runaway accretion may require special circumstances, such as a low viscosity in the gaseous disc.

At the same time, however, the Ca II emission lines from some WD systems are observed to have asymmetric shapes (Gänsicke et al. 2006, 2007). These have been interpreted as due to *non-circular* motions in the gaseous disc, with Gänsicke et al. (2006) for instance fitting the Ca II line profiles from WD SDSS 1228+1040 as arising from a disc with eccentricity $e \approx 0.02$. If this interpretation is correct, then the assumption of purely circular gas motion is not justified in at least some WD systems.

If the gas disc is eccentric (even if the origin of the eccentricity is unknown) then one must re-evaluate the drag force calculation from Section 2.1 to account for non-circular motions. In Appendix D, we carry out such a calculation, in particular demonstrating that in the small-e limit ($e \to 0$) the orbit-averaged azimuthal force can be written by analogy with equation (18) as $\langle f_a(r) \rangle_\varphi = A_e \Sigma_{\rm g}(r)$, see equation (D10), where now the coupling constant is

$$A_e = \frac{e^2}{8{\rm Re}_\star} \frac{r^2 \Omega^3}{c_{\rm s}}. \qquad (60)$$

[3] As shown in Fig. 3, our drag law underestimates aerodynamic coupling in the optically thin case. In reality, coupling is stronger and this may lower the disc lifetime to some extent.

The ratio of A_e to the coupling constant A_a defined by equation (19) is

$$\frac{A_e}{A_a} = \frac{e^2}{8}\left(\frac{\Omega r}{c_s}\right)^4. \quad (61)$$

As a result, even a small eccentricity of the gaseous streamlines $e \gtrsim (c_s/\Omega r)^2$ (which is about 10^{-6} at the inner disc edge) is sufficient for non-circular gas motions to dominate over the azimuthal velocity difference resulting due to gas pressure support for purposes of coupling the gaseous and solid discs.

Using equations (34) and (60) we can estimate the feedback parameter for coupling due to the non-circular gas motions:

$$\mathcal{F}_e = \frac{4A_{e,\rm in}R_{\rm in}}{\alpha_{\rm in}c_s^2} = \frac{e^2}{2\alpha_{\rm in}{\rm Re}_\star}\left(\frac{\Omega r}{c_s}\right)^3 \approx 30\left(\frac{\alpha_{\rm in}}{10^{-3}}\frac{{\rm Re}_\star}{10^2}\right)^{-1}\left(\frac{e}{10^{-4}}\right)^2\left(\frac{r}{0.2\,{\rm R}_\odot}\right)^{-3/2}, \quad (62)$$

where we have again adopted fiducial values for $\mu = 28m_{\rm p}$, $T_{\rm g} = 5000\,{\rm K}$ and $M_\star = 0.6\,{\rm M}_\odot$.

This expression shows that non-circular gas motions are extremely efficient at driving the runaway evolution of the debris discs, with even slightly eccentric ($e \sim 10^{-4}$) gas motions resulting in very strong feedback. In fact, this coupling may be *too* effective in the sense that $\mathcal{F} \gg 1$ implies a very short time-scale of $\sim t_{\rm s} = \mathcal{F}^{-1}t_\nu$ on which the particulate disc evolves due to coupling during the runaway. The duration of the build-up phase $t_{\rm run}$ is also lowered for $\mathcal{F} \gg 1$, see equation (59). Measurements of line asymmetries in WD gaseous discs typically imply $e \gg 10^{-4}$ if one interprets asymmetry as due to eccentric gas motions (e.g. $e \approx 0.02$ for SDSS 1228+1040: Gänsicke et al. 2006; and $e \approx 0.2$–0.4 for SDSS 0845+0855: Gänsicke et al. 2007). In the latter case, the inferred eccentricity would be so high as to result in relative velocity between the gas and particle discs of approximately hundreds of km s^{-1}. How such a highly supersonic velocity difference could be maintained in practice is not clear, unless the orbits of the solid particles are extremely closely aligned with the eccentric trajectory of the gas, which appears unlikely because of dissipative collisions between particles (see Section 6.4). It is furthermore unclear how the particle disc could avoid being destroyed by the enormous aerodynamic drag in this system, or by sputtering of the particle surfaces by the gas.

These considerations lead us to believe that the line asymmetries observed in the spectra of gaseous WD discs result not from actual non-circular gas motions, but rather as the result of a non-axisymmetric surface brightness over the face of the disc. Non-axisymmetric brightness patterns, resulting e.g. due to spiral waves or other instabilities which produce an azimuthally varying surface density distribution or line excitation conditions, could explain the observed line asymmetries without invoking highly non-circular gas motions. Hartmann et al. (2011) demonstrate that this is indeed possible.

To summarize, we conclude that the actual deviations of gas motions from purely circular in WD discs are probably not as dramatic as have been inferred based on eccentric disc models, and most likely correspond to $e \lesssim 10^{-4}$. Equation (62) nevertheless shows that even weakly non-circular gas motions could easily result in drag sufficient to produce runaway disc evolution, thus supporting the general picture outlined in R11b. Additional work is clearly required to identify what mechanisms are capable of driving such non-circular gas motions.

6.2 White dwarf magnetic field

We have thus far neglected the possible effects of the WD magnetic field on the disc evolution. If the WD field is sufficiently strong, it may, for instance, disrupt the gaseous disc above the WD surface, channelling matter on to the surface along the magnetic poles, as in magnetic cataclysmic variables.

Assuming that at large radii the WD magnetic field is dipolar $B(r) = B_\star(r/R_\star)^{-3}$ with a surface field strength $B_\star$, then the magnetosphere and disc stresses balance at the Alfvén radius $R_{\rm A}$ given by (e.g. Ghosh & Lamb 1978)

$$R_{\rm A} \simeq \left(\frac{3B_\star^2R_\star^6}{2\dot{M}\sqrt{GM_\star}}\right)^{2/7} \simeq 1.2\,{\rm R}_\odot\left(\frac{B_\star}{\rm kG}\right)^{4/7}\left(\frac{\dot{M}}{10^8\,{\rm g\,s^{-1}}}\right)^{-2/7} \times \left(\frac{R_\star}{10^{-2}\,{\rm R}_\odot}\right)^{12/7}\left(\frac{M_\star}{0.6\,{\rm M}_\odot}\right)^{-1/7}. \quad (63)$$

Equation (63) shows that for typical accretion rates in WD debris discs $\dot{M}_Z \sim 10^6$–$10^{10}\,{\rm g\,s^{-1}}$, fields as small as ∼0.1–1 kG are sufficient to affect the flow near the sublimation radius $R_{\rm in} \sim 0.2\,{\rm R}_\odot$.

The surface magnetic field strengths of isolated WDs inferred from Zeeman (spectro-)polarimetry show a wide range of values, from 'high field' WDs with $\gtrsim 10^4$ G (Wickramasinghe & Ferrario 2000), to only upper limits of $\lesssim$1–100 kG in most other systems (e.g. Schmidt & Smith 1995; Gänsicke et al. 2007). Overall, the distribution of field strengths appears to be well characterized by a power-law distribution ${\rm d}N/{\rm d}B \propto B^\alpha$ with index $\alpha \simeq -1.5$ for $B >$ 100 kG (Fabrika & Valyavin 1999). However, the peak and average of the distribution both occur at lower fields than can be measured and hence are not well constrained. Although few DZ WDs have measured magnetic fields, note that at least a few systems, G165-7 and G77-50, have strong surface fields $B_\star \sim 650$ kG (Dufour et al. 2006) and ∼120 kG (Farihi et al. 2011), respectively.

It thus seems possible that the WD magnetic fields could affect a significant fraction of debris discs.[4] If a dynamically important magnetic field threads the gaseous or solid disc, this may complicate the picture of disc evolution presented in this paper. If $R_\star \lesssim R_{\rm A} \lesssim R_{\rm s}$, then matter interior to the Alfvén radius is channelled directly on to the WD surface, creating an inner 'hole' in the gaseous disc. If $R_{\rm A} \gtrsim R_{\rm s}$, then matter may be placed on to field lines as soon as it sublimates at $r \approx R_{\rm s}$. Since viscous spreading is no longer required to carry away the angular momentum of the accreted gas (which is instead extracted by magnetic torques and used to spin-up the WD), then the picture of overlapping gas and solid discs, and the resulting model of runaway accretion developed in this paper, might no longer remain valid. An important caveat, however, is if small dust particles in the disc suppress the ionization fraction of the gas, as discussed earlier in this section. In this case, the magnetic field may not couple efficiently to the gaseous disc, negating the influence of even a strong field. A more detailed model of the coupled evolution of small dust, gas–field coupling and the MRI in the sublimation layer will be required to address the flow structure in this region and the resulting influence on the accretion evolution.

[4] Caveats include that (1) current measurements constrain the total surface field, of which the dipole may only be a minor component; (2) the magnetic field could be systematically lower in actively accreting systems if, for instance, the field is 'buried' by diamagnetic screening (e.g. Cumming, Zweibel & Bildsten 2001).

If the WD magnetic field is sufficiently strong to disrupt the gaseous disc, then it may also affect the rate of solid accretion via 'inductive' coupling (Drell, Foley & Ruderman 1965; Gurevich, Krylov & Fedorov 1978). Because the WD rotates at a different (typically much lower) angular velocity than the accretion disc, this differential rotation produces an electric field in the frame of the rotating particles of the order of $\boldsymbol{E} \simeq -(v_\phi/c) \times \boldsymbol{B}$, where $\boldsymbol{v}_\phi$ is the velocity at which the magnetic field sweeps through particles. If the WD magnetosphere is loaded with dense enough plasma supplying abundant free charges then this electric field not only polarizes debris particles but also induces a DC current through them. This current in turn couples to the magnetic field, resulting in the azimuthal drag force on the solid particles. The strength of this inductive coupling depends on the conductivity of particles and is rather uncertain. We leave a more detailed analysis of this coupling mechanism to future work.

6.3 Problem of condensation

The spatial coincidence of gaseous and particulate debris discs around WDs poses an interesting problem.[5] Quite generally, one expects that the debris particles and gas will have the same chemical composition, since the latter originates from the former (by evaporation in our model, or by sputtering as in Jura 2008). It is then not clear how two separate phases of the same material – solid and gaseous – can exist simultaneously in stable phase equilibrium.

Indeed, the temperature of the solid particles is necessarily below the sublimation temperature T_s, while the surrounding gas is likely to be hotter than T_s (Melis et al. 2010). Atoms of gas should stick upon colliding with the surface of debris particles, resulting in condensation with a probability equal to the accommodation coefficient $\alpha_{\rm acc} < 1$. The rate of condensation from the gas phase per unit area of the solid surface is $\sim\alpha_{\rm acc}\rho_g c_s \sim \alpha_{\rm acc}\Omega\Sigma_g$ (assuming a solid debris disc with $\tau_d \sim 1$), such that the gas disc should be depleted on a time-scale of $\sim\Omega^{-1}\alpha_{\rm acc}^{-1}$. Even if $\alpha_{\rm acc}$ is as small as $\sim 10^{-2}$ (its value is typically higher; see Leitch-Devlin & Williams 1985), then the entire gaseous disc should still condense within several hundred orbital time-scales. The latent heat released during this process may somewhat slow down the rate of condensation, but ultimately cannot prevent it.

Observations showing that the gaseous and solid components overlap in WD debris discs (Brinkworth et al. 2009; Melis et al. 2010) demonstrate that this simple logic is somehow flawed. However, at the moment we do not have a satisfactory explanation for this puzzle of condensation.

6.4 Production of metallic gas by particle collisions

Our work assumes that all metallic gas in the disc results from the sublimation of solids at the inner edge of the particulate disc (in Section 3.1 we allowed for the possibility of gas condensation at larger radii as described in Section 6.3, but we did not explore this possibility in detail). However, previous authors (Jura 2008; Farihi et al. 2009) have suggested that gas can also be produced by high-velocity collisions between solid particles within the debris disc. These authors argue that, due to the large orbital speed of approximately hundreds of km s^{-1}, even moderately non-circular particle motions (corresponding to orbital eccentricities as low as $\sim 10^{-2}$) result in particle collisions with sufficiently high velocity of several km s^{-1} to effectively sputter, or even vaporize, solids into metallic gas. This process of gas creation was envisioned to operate continuously throughout the entire solid disc, thereby naturally explaining the observed radial coincidence[6] between solid and gaseous discs (Melis et al. 2010).

We believe that this mechanism is unlikely to be an important source of gas production, even on time-scales short compared to the disc lifetime. Observations indicate (Jura 2003; Jura et al. 2007a) that WD debris discs are typically optically thick, i.e. $\tau_d \gtrsim 1$. It is well known (Goldreich & Tremaine 1978; Farihi et al. 2008) that under such circumstances the characteristic time-scale between the pairwise particle collisions is comparable to the local orbital period, which is less than an hour in the present context. If particles are indeed continuously being converted to gas via binary collisions, then the whole disc of solid debris should be converted into gas within just a handful of collision time-scales, i.e. approximately a day. This is in contradiction with the fact that the near-IR excesses observed around many WDs are persistent for at least decade-long time-scales.

Even if gas production via collisions is highly inefficient, such that only a small fraction of the solid mass is converted into gas in every collision (as would be necessary to extend the lifetime of the solid disc), then collisions are still incapable of providing a steady source of gas. This is because high relative velocities between particles are quickly damped (again, on a time-scale of several orbits) due to the inelastic nature of particle collisions (Goldreich & Tremaine 1978). As a result, the solid disc rapidly settles into a dynamically cold configuration, similar to the rings of Saturn (for which the particle velocity dispersion is only $\sim$0.01–0.1 cm s^{-1}; Cuzzi et al. 2010), thereby eliminating the possibility of additional destructive *high-velocity* particle collisions.

Despite these objections, collisional gas production is likely to be important during and immediately following the tidal disruption of the asteroid-like body by the WD, which could last for several orbital time-scales of the incoming body, i.e. approximately tens to hundreds of years. During this stage, collisions may occur between large solid objects at relative speeds of many km s^{-1}, resulting in a large fraction of the total solid mass being converted into gas. Some of this gas will re-condense on to the surfaces of surviving particles, with the rest accreting on to the WD on the (relatively short) viscous time-scale (see equation 2).

To summarize, the arguments presented above strongly argue against the possibility that *sustained, long-term* (comparable to the disc lifetime of $\sim 10^5$–10^6 yr) gas production in WD debris discs results from inelastic solid particle collisions.

7 SUMMARY

The growing number of 'debris discs' detected around WDs provides a unique opportunity to study the physics of the interaction between solid and gas discs in a way complementary to the study of normal debris discs around pre-main-sequence stars. As a likely repository for minor bodies originating from the outer stellar system, these discs also provide an indirect probe of the dynamics of planetary systems around evolved stars. As such, they also indirectly inform our knowledge of the fraction of the intermediate-mass stars harbouring planets.

[5] We are grateful to Bruce Draine for directing our attention to this issue.

[6] In our model, this overlap is naturally achieved as a result of viscous spreading of the gaseous disc (see Section 2).

Table 1. Summary of the key properties of different regimes of accretion in WD debris discs.[a]

Accretion regime	Disc lifetime $(t_\nu \times b_{\rm PR}^{-1}\mathcal{F}^{-1})^b$	Peak $\dot{M}_Z$ $(\dot{M}_{\rm PR,in})$
Optically thin ($\tau_{\rm d} \ll \zeta$)	$x_0^2 \times \zeta_{\rm in}$	$\zeta_{\rm in}^{-1}\tau_{\rm d}$
Optically thick ($\tau_{\rm d} \gg 1$)		
Weak feedback ($\mathcal{F} < 1$)	$x_0^2\Delta x \times \tau_{\rm d}$	x_0^{-1}
Strong feedback ($\mathcal{F} > 1$)	$x_0^3 \times \mathcal{F}^{-1}$	$x_0\Delta x \times \tau_{\rm d} b_{\rm PR}^{-1}\mathcal{F}^{-1}$

[a]Expressions are given in terms of (1) characteristic radius x_0 and radial thickness $\Delta x \lesssim x_0$ of the initial solid disc, in units of the inner edge of the disc $R_{\rm in} \approx R_{\rm s} \sim 0.2\,{\rm R}_\odot$ (equation 1); (2) viscous time t_ν at the inner disc edge (typically $\sim 10^3$ yr, depending on viscosity $\alpha_{\rm in}$, equation 2); (3) characteristic accretion rate $\dot{M}_{\rm PR,in}$ due to optically thick PR drag (typically $\sim 10^8\,{\rm g\,s^{-1}}$, equation 43); (4) dimensionless parameters introduced in Section 3.3, including the feedback parameter $\mathcal{F}$ (equations 34 and 44), PR parameters $b_{\rm PR}$ (typically $\sim 10^{-4}-1$, equations 31 and 45), and the incidence angle of WD radiation $\zeta_{\rm in}$ (typically $\sim$0.02, equation 31). [b] We express time in the useful combination $t_\nu b_{\rm PR}^{-1}\mathcal{F}^{-1}$, which takes on the numerical value $\sim 6 \times 10^4 (a/{\rm cm})$ yr for typical parameters (independent of the strength of the viscosity or the mechanism coupling solids and gas), where a is the characteristic particle size.

One of the biggest mysteries regarding known WD debris disc systems is the wide range of metal accretion rates, in particular those extending to much higher values than can be explained by PR drag alone (see Fig. 1). In this paper, we have begun to address this and other issues using global calculations of the coupled evolution of gaseous and solid components of WD debris discs. Table 1 summarizes the key properties of different regimes of accretion in WD debris discs. Our primary results are summarized as follows.

(i) The observed coexistence of gas and dust in WD debris discs (Melis et al. 2010) naturally results from viscous spreading of gas created at the sublimation radius.

(ii) Drag between the gaseous and solid discs leads to an enhanced accretion rate over that set by PR drag alone. Our results in Section 4 show that the disc evolution in the presence of strong aerodynamic drag is dramatically altered from cases without drag (see Figs 6–13). We confirm the mode of 'runaway' accretion predicted by R11b when the rate of drag-induced accretion exceeds the rate at which viscosity spreads gas away. The threshold for runaway is well described by the condition $\mathcal{F} \equiv t_\nu/t_{\rm s} \gtrsim 1$ (equation 34) for a variety of different configurations of solids (see also Appendix C).

(iii) The runaway process is characterized by two stages (Fig. 7): (1) an initial 'build-up' phase, during which an optically thick disturbance with $\tau_{\rm d} \sim 1$ moves inwards from the inner edge of the optically thick disc; (2) a 'runaway' phase characterized by super-exponential increase in the accretion rate, once $\tau_{\rm d} \sim 1$ is satisfied near the sublimation radius.

(iv) The predicted distribution of measured accretion rates given an ensemble of optically thick WD debris discs undergoing evolution leading to runaway is broadly consistent with the shape of the current observational sample (Figs 16–18). Most observed systems are predicted to have accretion rates in the range of $\dot{M}_Z \sim (0.1-1)\dot{M}_{\rm PR,in}$, but a smaller tail of the distribution comprising $\sim$10–20 per cent of systems should extend to higher accretion rates.

(v) Satisfying the runaway condition $\mathcal{F} > 1$ in WD debris discs requires a low value for the disc viscosity $\alpha_{\rm in} \lesssim 10^{-3}$–$10^{-4}$ and/or strong solid–gas coupling (equation 44). A low viscosity could result if the MRI is suppressed due to low ionization caused by the presence of small dust grains.

(vi) The runaway condition $\mathcal{F} > 1$ could also be satisfied even for higher viscosity if the strength of the solid–gas coupling is stronger than our baseline model for aerodynamic drag presented in Section 2.1. In Section 6.1 and Appendix D we show that even a mildly eccentric gaseous disc $e \gtrsim 10^{-4}$ results in a stronger drag force than our baseline model. These results also suggest that the observed asymmetries in WD emission lines are unlikely to result from highly eccentric discs, but instead may result from non-axisymmetric disturbances in the disc surface brightness (e.g. spiral wave patterns).

(vii) The disc lifetime in the runaway accretion model is set by the delay time-scale during the 'build-up' phase $t_{\rm life} \approx t_{\rm run}$ (equation 50). Reconciling this lifetime with the observational upper limits on the disc lifetime $t_{\rm life} < 10^5$–10^6 yr places an upper limit $a \lesssim$ several cm on the characteristic particle size (equation 59).

(viii) The steady-state assumption commonly adopted to calculate WD metal accretion rates (equation 55) may be inaccurate when the settling time of metals in the WD convective zone $t_{{\rm set},i} \gg 10t_\nu$, resulting in some cases in an overestimate or underestimate of the true instantaneous accretion rate by an order of magnitude or more (Fig. 14). This is a possible explanation for even heavily metal-rich WDs with no current IR excess in cases for which the metal diffusion time is comparable to the disc lifetime.

ACKNOWLEDGMENTS

BDM is supported by NASA through Einstein Postdoctoral Fellowship grant number PF9-00065 awarded by the Chandra X-ray Center, which is operated by the Smithsonian Astrophysical Observatory for NASA under contract NAS8-03060. Financial support for RRR is provided by the Sloan Foundation, NASA via grant NNX08AH87G and NSF via grant AST-0908269.

REFERENCES

Bergeron P., Saumon D., Wesemael F., 1995, ApJ, 443, 764
Bochkarev K. V., Rafikov R. R., 2011, ApJ, 741, 36 (BR11)
Brandenburg A., 2003, in Ferriz-Mas A., Núñez M., eds, Advances in Nonlinear Dynamics. Taylor and Francis, London, p. 269
Brinkworth C. S., Gänsicke B. T., Marsh T. R., Hoard D. W., Tappert C., 2009, ApJ, 696, 1402
Chu Y.-H. et al., 2011, AJ, 142, 75
Coleman G. N., Ferziger J. H., Spalart P. R., 1990, J. Fluid Mech., 213, 313
Cumming A., Zweibel E., Bildsten L., 2001, ApJ, 557, 958
Cuzzi J. N., Dobrovolskis A. R., Champney J. M., 1993, Icarus, 106, 102
Cuzzi J. N. et al., 2010, Sci, 327, 1470
Daisaka H., Tanaka H., Ida S., 2001, Icarus, 154, 296
Davis S. W., Stone J. M., Pessah M. E., 2010, ApJ, 713, 52
Debes J. H., Sigurdsson S., 2002, ApJ, 572, 556
Debes J. H., Hoard D. W., Wachter S., Leisawitz D. T., Cohen M., 2011a, ApJS, 197, 38
Debes J. H., Hoard D. W., Kilic M., Wachter S., Leisawitz D. T., Cohen M., Kirkpatrick J. D., Griffith R. L., 2011b, ApJ, 729, 4
Debes J., Walsh K., Stark C., 2012, ApJ, 747, 148
Dobrovolskis A. R., Dacles-Mariani J. S., Cuzzi J. N., 1999, J. Geophys. Res., 104, 30805
Drell S. D., Foley H. M., Ruderman M. A., 1965, J. Geophys. Res., 70, 3131
Dufour P., Bergeron P., Schmidt G. D., Liebert J., Harris H. C., Knapp G. R., Anderson S. F., Schneider D. P., 2006, ApJ, 651, 1112
Dufour P., Kilic M., Fontaine G., Bergeron P., Lachapelle F.-R., Kleinman S. J., Leggett S. K., 2010, ApJ, 719, 803
Duncan M. J., Lissauer J. J., 1998, Icarus, 134, 303

Ehrenreich D. et al., 2011, A&A, 525, A85
Fabrika S., Valyavin G., 1999, in Solheim S.-E., Meistas E. G., eds, ASP Conf. Ser. Vol. 169, 11th European Workshop on White Dwarfs. Astron. Soc. Pac., San Francisco, p. 214
Faller A. J., 1963, J. Fluid Mech., 15, 560
Farihi J., Zuckerman B., Becklin E. E., 2008, ApJ, 674, 431
Farihi J., Jura M., Zuckerman B., 2009, ApJ, 694, 805
Farihi J., Barstow M. A., Redfield S., Dufour P., Hambly N. C., 2010a, MNRAS, 404, 2123
Farihi J., Jura M., Lee J.-E., Zuckerman B., 2010b, ApJ, 714, 1386
Farihi J., Dufour P., Napiwotzki R., Koester D., 2011, MNRAS, 413, 2559
Fleming T. P., Stone J. M., Hawley J. F., 2000, ApJ, 530, 464
Frank J., King A., Raine D. J., 2002, Accretion Power in Astrophysics, 3rd edn. Cambridge Univ. Press, Cambridge
Friedjung M., 1985, A&A, 146, 366
Fromang S., Papaloizou J., 2007, A&A, 476, 1113
Gänsicke B. T., Marsh T. R., Southworth J., Rebassa-Mansergas A., 2006, Sci, 314, 1908
Gänsicke B. T., Marsh T. R., Southworth J., 2007, MNRAS, 380, L35
Gänsicke B. T., Koester D., Marsh T. R., Rebassa-Mansergas A., Southworth J., 2008, MNRAS, 391, L103
Ghosh P., Lamb F. K., 1978, ApJ, 223, L83
Girven J., Brinkworth C. S., Farihi J., Gänsicke B. T., Hoard D. W., Marsh T. R., Koester D., 2012, ApJ, ArXiv e-prints
Goldreich P., Tremaine S. D., 1978, Icarus, 34, 227
Goldreich P., Ward W. R., 1973, ApJ, 183, 1051
Gradshteyn I. S., Ryzhik I. M., Jeffrey A., Zwillinger D., 2007, eds, Table of Integrals, Series, and Products. Elsevier Academic Press, Waltham, Massachusetts
Graham J. R., Matthews K., Neugebauer G., Soifer B. T., 1990, ApJ, 357, 216
Gurevich A. V., Krylov A. L., Fedorov E. N., 1978, Z. Eksp. Teor. Fiz., 75, 2132
Hansen B. M. S., Kulkarni S., Wiktorowicz S., 2006, AJ, 131, 1106
Hartmann S., Nagel T., Rauch T., Werner K., 2011, A&A, 530, A7
Johansen A., Oishi J. S., Mac Low M.-M., Klahr H., Henning T., Youdin A., 2007, Nat, 448, 1022
Jura M., 2003, ApJ, 584, L91
Jura M., 2006, ApJ, 653, 613
Jura M., 2008, AJ, 135, 1785
Jura M., Farihi J., Zuckerman B., 2007a, ApJ, 663, 1285
Jura M., Farihi J., Zuckerman B., Becklin E. E., 2007b, AJ, 133, 1927
Jura M., Muno M. P., Farihi J., Zuckerman B., 2009a, ApJ, 699, 1473
Jura M., Farihi J., Zuckerman B., 2009b, AJ, 137, 3191
Kilic M., Redfield S., 2007, ApJ, 660, 641
Kilic M., von Hippel T., Leggett S. K., Winget D. E., 2005, ApJ, 632, L115
Kilic M., Farihi J., Nitta A., Leggett S. K., 2008, AJ, 136, 111
King A. R., Pringle J. E., Livio M., 2007, MNRAS, 376, 1740
Klein B., Jura M., Koester D., Zuckerman B., Melis C., 2010, ApJ, 709, 950
Koester D., 2009, A&A, 498, 517
Koester D., Wilken D., 2006, A&A, 453, 1051
Leitch-Devlin M. A., Williams D. A., 1985, MNRAS, 213, 295
Lin D. N. C., Papaloizou J. C. B., 1996, ARA&A, 34, 703
Melis C., Jura M., Albert L., Klein B., Zuckerman B., 2010, ApJ, 722, 1078
Metzger B. D., Piro A. L., Quataert E., 2009, MNRAS, 396, 304
Mullally F., Kilic M., Reach W. T., Kuchner M. J., von Hippel T., Burrows A., Winget D. E., 2007, ApJS, 171, 206
Paquette C., Pelletier C., Fontaine G., Michaud G., 1986, ApJS, 61, 197
Pringle J. E., 1981, ARA&A, 19, 137
Rafikov R. R., 2011a, ApJ, 732, L3 (R11a)
Rafikov R. R., 2011b, MNRAS, 416, L55 (R11b)
Ruden S. P., 2004, ApJ, 605, 880
Schmidt G. D., Smith P. S., 1995, ApJ, 448, 305
Shakura N. I., Sunyaev R. A., 1973, A&A, 24, 337
Takeda T., Ida S., 2001, ApJ, 560, 514
Tanaka T., 2011, MNRAS, 410, 1007
von Hippel T., Kuchner M. J., Kilic M., Mullally F., Reach W. T., 2007, ApJ, 662, 544
Weidenschilling S. J., 1977, MNRAS, 180, 57
Whipple F. L., 1972, in Elvius A., ed., From Plasma to Planet on Certain Aerodynamic Processes for Asteroids and Comets. Wiley, New York, p. 211
Wickramasinghe D. T., Ferrario L., 2000, PASP, 112, 873
Wisdom J., Tremaine S., 1988, AJ, 95, 925
Wyatt M. C., 2008, ARA&A, 46, 339
Xu S., Jura M., 2012, ApJ, 745, 88
Youdin A. N., Goodman J., 2005, ApJ, 620, 459
Zuckerman B., Becklin E. E., 1987, Nat, 330, 138
Zuckerman B., Koester D., Melis C., Hansen B. M., Jura M., 2007, ApJ, 671, 872
Zuckerman B., Melis C., Klein B., Koester D., Jura M., 2010, ApJ, 722, 725

APPENDIX A: MASS ACCRETION DUE TO COLLISIONAL VISCOSITY

Here we evaluate the role of 'internal' sources of viscosity within the particulate disc, similar to those thought to characterize the evolution of the rings of Saturn, on the rate of solid accretion in WD debris discs. Angular momentum transport in a dense ring is caused by three effects (Wisdom & Tremaine 1988; Takeda & Ida 2001): (1) translational transport due to the particle motions; (2) collisional transport; and (3) transport due to the gravitational torques, which are important only when self-gravity is important.

According to Daisaka, Tanaka & Ida (2001), the efficiency of gravitational transport is determined by two parameters: (1) the optical depth of the particulate disc $\tau_{\rm d}$ (equation 3) and (2) the ratio of the mutual Hill radius $r_{\rm h} \equiv r(2m_{\rm p}/3M_\star)^{1/3}$ to twice the particle radius a:

$$r_{\rm h}^* \equiv \frac{r_{\rm h}}{2a} = \left(\frac{\pi}{9}\frac{\rho}{M_\star}\right)^{1/3} r \approx 0.1\left(\frac{\rho_{\rm d}}{2.5\,{\rm g\,cm^{-3}}}\frac{0.6\,{\rm M_\odot}}{M_\star}\right)^{1/3}\left(\frac{r}{0.2\,{\rm R_\odot}}\right), \quad \text{(A1)}$$

where $m_{\rm p} = (4\pi/3)\rho_{\rm d}a^3$, $\rho_{\rm d}$ and r are the particle mass, density and distance from the WD, respectively. Note that $r_{\rm h}^*$ is independent of the particle mass.

Equation (A1) shows that $r_{\rm h}^* \lesssim 0.5$ is typically satisfied for the range of radii $r \lesssim {\rm R_\odot}$ relevant to WD debris discs. In this regime, gravitational transport can be neglected provided that (Daisaka et al. 2001)

$$\tau_{\rm d} \lesssim \tau_{\rm sg} \approx \frac{0.08}{\left(r_{\rm h}^*\right)^3} \approx 60\left(\frac{M_\star}{0.6\,{\rm M_\odot}}\frac{2.5\,{\rm g\,cm^{-3}}}{\rho_{\rm d}}\right)\left(\frac{0.2\,{\rm R_\odot}}{r}\right)^3. \quad \text{(A2)}$$

If gravitational transport is negligible then internal transport is instead dominated by the collisional viscosity $\nu \approx a^2\Omega\tau_{\rm d}$ (Daisaka et al. 2001), where $\Omega = (GM_\star/r^3)^{1/2}$. The resulting mass flux can be estimated as

$$\dot{M}_Z = 3\pi\nu\Sigma_{\rm d} = 3m_{\rm p}\tau_{\rm d}^2\Omega \approx 60{\rm g\ s^{-1}}\left(\frac{m_{\rm p}}{1\,{\rm g}}\right)\left(\frac{\tau_{\rm d}}{60}\right)^2\left(\frac{M_\star}{0.6\,{\rm M_\odot}}\right)^{1/2}\left(\frac{r}{0.2\,{\rm R_\odot}}\right)^{-3/2}. \quad \text{(A3)}$$

Equation (A3) shows that in order to explain typical values $\dot{M}_Z \sim 10^8\,{\rm g\,s^{-1}}$ of the accretion rates on to metal-rich WDs, then for[7] $\tau_{\rm d} \sim 60$ one requires a typical particle mass $m_{\rm p} \sim 10^7$ g, corresponding to an object of size $a \gtrsim 1$ m. Obviously, particles of size

[7] For $\tau_{\rm d} \lesssim 1$, as characterize e.g. Saturn's rings, one would need $\gtrsim$10 m particles to achieve the same value of $\dot{M}_Z$.

$a \sim 1$ m in a disc with optical depth $\tau_{\rm d} \sim 60$ cannot reside in a monolayer configuration; rather, the vertical thickness of the disc must be $\sim$100 m, thus requiring a total solid mass $\sim(4\pi/3)\rho_{\rm d} a r^2 \tau_{\rm d} \approx 10^{25}$ g (assuming characteristic disc size $r = 0.2\,{\rm R}_\odot$). This mass is similar to that of a single 2000-km basaltic asteroid, which is significantly higher than the total mass of high-Z elements typically inferred to pollute metal-rich WDs (Farihi et al. 2010a).

Explaining the highest inferred values of $\dot{M}_Z \sim 10^{10}$–10^{11} g s^{-1} requires even larger disc particles ($\sim$10 m) and, hence, even more massive discs. In principle, the ring viscosity is enhanced if $\tau_{\rm d}$ is sufficiently high that equation (A2) is violated; when self-gravity becomes important, the viscosity instead becomes $\nu \propto \tau_{\rm d}^3$ (Daisaka et al. 2001). However, the required disc mass in this case approaches that of a terrestrial size body, an unlikely explanation for all WDs with high $\dot{M}_Z$. We conclude that viscosity due to internal stresses within the particulate ring is unlikely to play an important role in the majority of metal-rich WDs. A similar conclusion was reached by Farihi et al. (2008), who also estimated accretion times based on an analogy with planetary rings, finding that typically they greatly exceed the WD cooling time-scale.

APPENDIX B: EVOLUTION OF ACCRETION DISCS WITH MASS SOURCES/SINKS: ANALYTICAL SOLUTIONS

Here we analyse equation (27) to derive some general results for the viscous evolution of an accretion disc with sources or sinks of mass and power-law dependence of viscosity on radius

$$\nu = \nu_0 r^n, \tag{B1}$$

but without sources or sinks of the angular momentum, i.e. $\Lambda = 0$ in equation (27). Other analytic work on the evolution of accretion discs in the presence of mass sources/sinks (for the case of $n = 1$) can be found in Ruden (2004).

The initial condition for the disc evolution is

$$\Sigma_{\rm g}(r, t = 0) = \Sigma_{\rm g,0}(r). \tag{B2}$$

Power-law viscosity is realized in the conventional model of α-viscosity (Shakura & Sunyaev 1973) provided that the gas temperature $T_{\rm g}$ has a power-law dependence on radius:

$$\nu(r) = \frac{\alpha c_{\rm s}^2}{\Omega} = \alpha \frac{k_{\rm B} T_{\rm g}(r) r^{3/2}}{\mu\sqrt{G M_\star}}. \tag{B3}$$

In particular, if $T_{\rm g}(r) =$ constant, then $n = 3/2$. If $T_{\rm g}(r) \propto r^{-1/2}$, as expected for optically thin gas in equilibrium with stellar heating, then $n = 1$.

Following Tanaka (2011) and introducing new time-like and spatial coordinates T (not to be confused with temperature) and w,

$$T \equiv 3\nu_0 t, \quad w(r) \equiv \frac{2}{2-n} r^{1-n/2}, \tag{B4}$$

and looking for a solution in the form

$$\Sigma_{\rm g}(r, t) = r^{-n-1/4} \sigma_{\rm g}(w, T), \tag{B5}$$

equation (27) can be transformed to

$$\frac{\partial \sigma_{\rm g}}{\partial T} = \frac{\partial^2 \sigma_{\rm g}}{\partial w^2} + \frac{1}{w}\frac{\partial \sigma_{\rm g}}{\partial w} - \frac{l^2}{w^2}\sigma_{\rm g} + \Psi(w, T), \quad l = \frac{1}{2(2-n)},$$
$$\Psi(w, T) \equiv [r(w)]^{n+1/4} \frac{S_{\rm g}(r(w), T)}{3\nu_0}. \tag{B6}$$

We now introduce Hankel transforms $\tilde{F} = \left\{\tilde{\sigma}_{\rm g}(k, T), \tilde{\Psi}(k, T), \tilde{\Sigma}_{\rm g,0}(k)\right\}$ for each of the functions $\tilde{F} = \left\{\sigma_{\rm g}, \Psi, \Sigma_{\rm g,0}\right\}$ according to

$$\tilde{F}(k, T) = \int_0^\infty F(w, T) J_l(kw) w {\rm d}w,$$
$$F(w, T) = \int_0^\infty \tilde{F}(k, T) J_l(kw) k {\rm d}k. \tag{B7}$$

Plugging these relations into (B6), one arrives at the following simple differential equation for $\tilde{\sigma}_{\rm g}(k, T)$:

$$\frac{\partial \tilde{\sigma}_{\rm g}(k, T)}{\partial T} + k^2 \tilde{\sigma}_{\rm g}(k, T) = \tilde{\Psi}(k, T), \tag{B8}$$

with the initial condition

$$\tilde{\sigma}_{\rm g}(k, T = 0) = \tilde{\Sigma}_{\rm g,0}(k). \tag{B9}$$

Solving this equation and performing inverse Hankel transform on $\tilde{\sigma}_{\rm g}$, we obtain

$$\Sigma_{\rm g}(r, t) = r^{-n-1/4} \int_0^\infty \left[\tilde{\Sigma}_{\rm g,0}(k) + \int_0^T \tilde{\Psi}(k, T') {\rm e}^{k^2 T'} {\rm d}T'\right] \times {\rm e}^{-k^2 T} J_l(kw(r)) k {\rm d}k. \tag{B10}$$

We can further simplify this solution by plugging in the expressions for $\tilde{\Sigma}_{\rm g,0}$ and $\tilde{\Psi}$ from equation (B7), rearranging the order of integration and using integral 6.633(2) from Gradshteyn et al. (2007). This gives us

$$\Sigma_{\rm g}(r, t) = \int_0^\infty \left(\frac{r(w')}{r}\right)^{n+1/4} \left[\Sigma_{\rm g,0}(w') G(w(r), w', T) + \int_0^T \frac{S_{\rm g}(w', T')}{3\nu_0} G(w(r), w', T - T') {\rm d}T'\right] w' {\rm d}w', \tag{B11}$$

where

$$G(w, w', z) \equiv \frac{1}{2z} \exp\left(-\frac{w^2 + w'^2}{4z}\right) I_l\left(\frac{ww'}{2z}\right), \tag{B12}$$

and $T(t)$ and $w(r)$ are given by equation (B4).

B1 Singular mass source

For our current set-up (sublimation at a single radius) it is useful to consider the situation when the injection of mass happens over a small radial span of the disc at $r = R_{\rm in}$, so that one can write

$$S_{\rm g}(r, t) = S_t(t)\delta(r - R_{\rm in}), \quad S_t(t) = \frac{\dot{M}(r = R_{\rm in}, t)}{2\pi R_{\rm in}}, \tag{B13}$$

see equation (29). For simplicity, we will assume that initially the disc does not contain any mass, i.e. $\Sigma_{\rm g,0} = 0$. Abandoning this assumption would amount to including the first term in equation (B11) into the consideration.

Plugging equation (B13) into equation (B11) and introducing $w_0 \equiv w(R_{\rm in})$, one finds

$$\Sigma_{\rm g}(r, t) = \frac{2}{2-n} \frac{R_{\rm in}^{5/4} r^{-n-1/4}}{3\nu_0} \int_0^T S_t(T') G(w(r), w_0, T - T') {\rm d}T'. \tag{B14}$$

One can obtain a simple solution for $\Sigma_{\rm g}(r, t)$ at late times $T \gg w_0^2$ under the assumption that $S_t(T)$ varies slowly. In this case we can take $S_t(T)$ to be approximately constant and take it out of the integral in equation (B14). Then one gets

$$\Sigma_{\rm g}(r, t) = \frac{2S_t}{2-n} \frac{R_{\rm in}^{5/4} r^{-n-1/4}}{3\nu_0} \int_0^T G(w(r), w_0, z) {\rm d}z \approx \frac{S_t R_{\rm in}^{5/4} r^{-n-1/4}}{3(2-n)\nu_0} \int_0^\infty \frac{{\rm d}z}{z} \exp\left(-\frac{w^2 + w_0^2}{4z}\right) I_l\left(\frac{ww_0}{2z}\right). \tag{B15}$$

Taking the last integral with the aid of relation

$$\int_0^\infty \frac{\mathrm{d}u}{u} \mathrm{e}^{-\lambda u} I_\nu(u) = \frac{1}{\nu}\left(\lambda + \sqrt{\lambda^2 - 1}\right)^{-\nu}, \tag{B16}$$

one finds that

$$\Sigma_\mathrm{g}(r,t) = \frac{2S_t}{3\nu_0}\frac{R_\mathrm{in}^{3/2}}{r^{n+1/2}}, \quad r > R_\mathrm{in},$$
$$= \frac{2S_t}{3\nu_0}\frac{R_\mathrm{in}}{r^n}, \quad r < R_\mathrm{in}. \tag{B17}$$

With this expression for the surface density, one can easily determine the mass accretion rate through the disc:

$$\dot{M}(r) = 6\pi r^{1/2}\frac{\partial}{\partial r}\left(\nu\Sigma r^{1/2}\right) = 0, \quad r > R_\mathrm{in}, \tag{B18}$$

while for $r < R_\mathrm{in}$ one finds $\dot{M}(r) = 2\pi S_t R_\mathrm{in}$. Thus, all of the mass injected at R_in goes towards the central mass at late times.

APPENDIX C: COUPLED EVOLUTION IN THE ABSENCE OF MOMENTUM FEEDBACK ON THE GASEOUS DISC

The goal of this appendix is to gain analytical insight into the coupled evolution of gaseous and solid WD discs, which are linked by mass exchange due to the evaporation of solids, as expressed by the source term in equation (29).

Here we account for the effect of gas drag on the evolution of the surface density of solids (as we do in Section 4), *but we neglect the back-reaction of the drag force on the gas disc evolution*, assuming that its effect is small compared to that of the viscous stresses. With this simplification the evolution of the gas disc can be studied using the results of Appendix B, provided that the viscosity obeys the power-law ansatz (equation B1). Fig. C1 shows a comparison between the mass accretion rate $\dot{M}_Z$ computed with and without the back-reaction of the aerodynamic drag on the gaseous disc. The similar qualitative evolution in both cases justifies our assumption that the back-reaction force on the gas disc can be neglected to first order.

Another important assumption we make here is that the surface density of solids at R_in is sufficiently high that $\tau_\mathrm{d}(R_\mathrm{in}, t) \gtrsim 1$ is satisfied at all times. This approximation is likely to be valid only during the late stages of the disc evolution, as illustrated in Figs 6(a) and 12. Thus, the model we present below does not capture the early, 'build-up' phase of the gaseous disc evolution, but it should work well at late times, during the runaway phase. This important simplification makes it possible to treat the evolution of the gas disc analytically, separate from the calculation of the solid disc evolution.

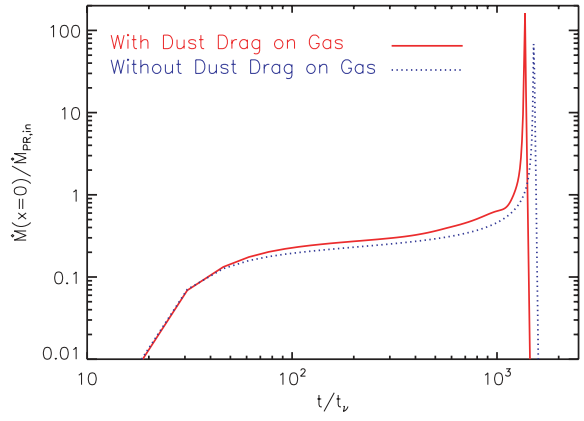

Figure C1. Comparison of the evolution of the gas accretion rate $\dot{M}_Z(t)$ in two cases for otherwise fully identical simulations: when the back-reaction of the aerodynamic drag on the gas disc is not included (dotted line) and when it is fully accounted for (solid line). Note that only small quantitative differences distinguish the behaviour of $\dot{M}_Z(t)$ in the two cases.

Using equations (21)–(24), (26) and (B13) one obtains the following expression for the intensity of the mass source feeding the gaseous disc:

$$S_t(t) = \frac{\dot{M}_\mathrm{PR,in}}{2\pi R_\mathrm{in}} + \frac{\eta|\eta|}{2}\frac{R_\mathrm{in}}{t_\mathrm{s}}\Sigma_\mathrm{g}(R_\mathrm{in}, t), \tag{C1}$$

where we have assumed that $r = R_\mathrm{in}$ and that $\tau_\mathrm{d}(R_\mathrm{in}, t) \gtrsim 1$.

This expression, coupled with the solution in equation (B14), provides a closed set of equations for the evolution of $\Sigma_\mathrm{g}(r,t)$ which can be computed numerically. Note that a knowledge of $\Sigma_\mathrm{d}(r,t)$ is not required to calculate $\Sigma_\mathrm{g}(r,t)$ as long as $\tau_\mathrm{d}(R_\mathrm{in}, t) \gtrsim 1$. This is because the mass flux of solid debris at R_in saturates at the value independent of $\tau_\mathrm{d}(R_\mathrm{in}, t)$ when the disc of solids is optically thick.

To demonstrate the conditions under which runaway behaviour becomes possible, we concentrate on evaluating the time evolution of Σ_g at R_in only. By substituting equation (C1) into equation (B14), setting $r = R_\mathrm{in}$, and casting all variables into dimensionless form with the aid of equations (31)–(35), one obtains the following integral equation for the evolution of the gas optical depth at the inner edge of the disc $\tau_\mathrm{g,in}(t) \equiv \tau_\mathrm{g}(R_\mathrm{in}, t)$:

$$\tau_\mathrm{g,in}(\tilde{t}) = \mathcal{F}\frac{2-n}{4}\int_0^{\tilde{t}}\left[\eta|\eta|\tau_\mathrm{g,in}(\tilde{t}') + b_\mathrm{PR}\right] \times \tilde{G}\left(\frac{3(2-n)^2}{4}(\tilde{t}-\tilde{t}')\right)\mathrm{d}\tilde{t}', \tag{C2}$$

where

$$\tilde{G}(z) \equiv \frac{1}{2z}\exp\left(-\frac{1}{2z}\right) I_l\left(\frac{1}{2z}\right). \tag{C3}$$

Note that $t_\nu = R_\mathrm{in}^{2-n}/\nu_0$ for the power-law viscosity (B1).

Our numerical results presented in Section 4 demonstrate that there are two possibilities for the gas disc evolution: either (1) Σ_g saturates at essentially a constant level on time-scales long compared to t_ν or (2) it grows with time in a runaway fashion. In both cases, the behaviour of Σ_g is determined primarily by the most recent history of the disc and is largely insensitive to conditions in the distant past. This allows us to extend the lower limit of integration in equation (C2) to $-\infty$ for $\tilde{t} \gg 1$. This results (upon an obvious change of variables) in the following equation describing the late-time behaviour of Σ_g:

$$\tau_\mathrm{g,in}(\tilde{t}) = \mathcal{F}\frac{2-n}{4}\int_0^{\infty}\left[\eta|\eta|\tau_\mathrm{g,in}(\tilde{t}-z) + b_\mathrm{PR}\right] \times \tilde{G}\left(\frac{3(2-n)^2}{4}z\right)\mathrm{d}z. \tag{C4}$$

In the case of orderly behaviour, $\tau_\mathrm{g,in}$ saturates at the constant level, such that the expression in brackets in equation (C4) can be taken out of the integral. Using the fact that $\int_0^\infty \tilde{G}(z)\mathrm{d}z = 1/(2l) = (2-n)$, one then finds that $\tau_\mathrm{g,in}$ saturates at the value

$$\tau_\mathrm{g,in} \approx \frac{\mathcal{F}}{3}\frac{b_\mathrm{PR}}{1-(\mathcal{F}/3)\eta|\eta|}. \tag{C5}$$

This result and the whole picture of the orderly disc evolution are applicable only if

$$\mathcal{F} < \frac{3}{\eta|\eta|}. \tag{C6}$$

In the opposite case of runaway behaviour, the first term in brackets in equation (C4) rapidly comes to dominate over the second one. In this case, the equation then has an exponentially growing solution $\tau_{\rm g,in}(\tilde{t}) \propto {\rm e}^{\mu\tilde{t}}$, with a constant $\mu > 0$ which satisfies the transcendental equation

$$1 = \mathcal{F}\eta|\eta|\frac{2-n}{4}\int_0^\infty {\rm e}^{-\mu z}\tilde{G}\left(\frac{3(2-n)^2}{4}z\right){\rm d}z. \tag{C7}$$

It is easy to check that this equation has a positive solution (and the system evolves in a runaway fashion) only if

$$\mathcal{F} > \frac{3}{\eta|\eta|}, \tag{C8}$$

which is the condition opposite to that in equation (C6). In particular, if we assume $n = 3/2$, which according to equation (B3) corresponds to $T_{\rm g}(r) =$ constant profile in the gas disc, then equations (40) and (B17) imply that $\eta = 7/4$, such that $\mathcal{F} > 48/49 \approx 1$ is needed for the disc to evolve in a runaway fashion.

The upshot of this calculation is that, even in this simple model of the coupled disc evolution, runaway behaviour becomes possible only when the feedback parameter $\mathcal{F}$ exceeds some critical value close to unity, given by equation (C8). We emphasize that despite the simplifications made in this section, the model presented is still fully global, as opposed to the treatment of R11b. Nevertheless, our result in equation (C8) is in agreement with the runaway condition $\mathcal{F} \gtrsim 1$ derived entirely from local considerations by R11b. And as we demonstrate in Section 4, the general result given by equation (C8) remains valid even for the more complicated global models of the system, e.g. in which the back-reaction of the aerodynamic drag on the gas disc is self-consistently included and the possibility that $\tau_{\rm g}(R_{\rm in}) \lesssim 1$ is allowed.

APPENDIX D: SOLID–GAS COUPLING IN ECCENTRIC DISCS

We assume for simplicity that the streamlines in the gaseous disc are confocal ellipses (with foci coinciding with the WD position) with eccentricity e being the same for all streamlines, and with apsidal lines pointing in the same direction (see Fig. D1). There is no reason to believe that this geometric model captures all details of non-circular gas motion in real circum-WD discs – we adopt it here just to facilitate our calculations. Despite its simplicity, this model is sufficient to illustrate the importance of even moderately non-circular gas motions.

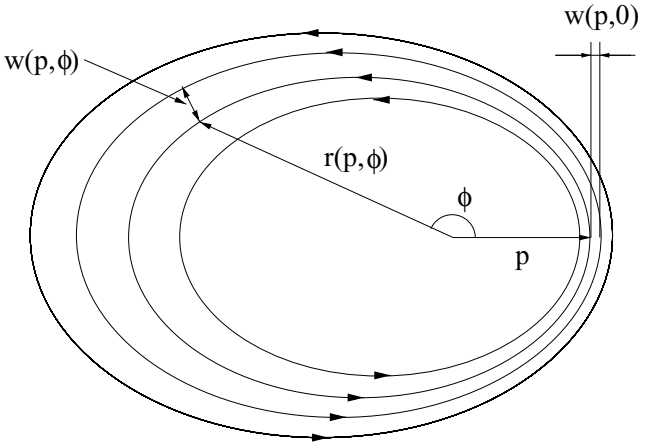

Figure D1. Schematic representation of the gas flow in an eccentric disc used to compute the aerodynamic drag between the solid and eccentric gaseous discs. See text for details.

We characterize each gas streamline by its periastron distance $p = a(1-e)$, where a is the semimajor axis of a corresponding streamline. Due to the non-circular shape of the streamlines, the surface density of gas varies as it travels along a given streamline. We characterize this variation by assuming that surface density is a function of p and φ – the polar angle of the radius vector $\boldsymbol{r}$ at a given point on a streamline with respect to the apsidal line (see Fig. D1). The dependence of $\Sigma_{\rm g}$ on p characterizes the radial profile of the surface density.

We denote $w(p,\varphi)$ as the (small) distance between the two neighbouring streamlines (width of the flux tube confined by these streamlines) separated by the (small) distance $w(p,0)$ along the apsidal line. Clearly,

$$\frac{w(p,\varphi)}{w(p,0)} = |\nabla p(r,\varphi)|^{-1} = \frac{1+e}{\left(1+2e\cos\varphi+e^2\right)^{1/2}}, \tag{D1}$$

where we have used the equation for elliptical orbit in polar coordinates

$$p = r\frac{1+e\cos\varphi}{1+e}. \tag{D2}$$

The gas surface density at periastron $\Sigma_{\rm g}(p,0)$ is related to the density $\Sigma_{\rm g}(p,\varphi)$ at a different location along the same streamline via the continuity equation $\Sigma_{\rm g}(p,\varphi)v(p,\varphi)w(p,\varphi) = \Sigma_{\rm g}(p,0)v(p,0)w(p,0)$, where

$$v(p,\varphi) = \frac{\Omega(p)p}{1-e}\left(\frac{1+2e\cos\varphi+e^2}{1-e^2}\right)^{1/2} \tag{D3}$$

is the Keplerian velocity along the streamline (we neglect the modification of the gas rotation profile by pressure support). Here, $\Omega(p)$ is the value of Ω corresponding to the semimajor axis $a = p/(1-e)$. Using equations (D1) and (D3) we obtain

$$\Sigma_{\rm g}(p,\varphi) = \Sigma_{\rm g}(p,0)\frac{(1+e)^2}{1+2e\cos\varphi+e^2}. \tag{D4}$$

Now, let us consider a ring of particulate debris with radius r. An elliptic streamline passing through a point (r,φ) on this ring has a periastron distance $p(r,\varphi)$ given by equation (D2). The azimuthal velocity of gas passing through (r,φ) is given by

$$\begin{aligned} v_{\varphi,{\rm g}}(r,\varphi) &= \left(\frac{GM_\star(1-e)}{p(r,\varphi)}\right)^{1/2}\frac{1+e\cos\varphi}{\sqrt{1-e^2}} \\ &= \left(\frac{GM_\star}{r}\right)^{1/2}(1+e\cos\varphi)^{1/2}, \end{aligned} \tag{D5}$$

where we have again neglected pressure support in the gas disc. The relative azimuthal velocity between the gas and particles at point (r,φ) is then given by

$$v_{\varphi,{\rm rel}} = \left(\frac{GM_\star}{r}\right)^{1/2}\left[1-(1+e\cos\varphi)^{1/2}\right], \tag{D6}$$

i.e. the gas rotates faster (slower) than particles at $\varphi = 0$ ($\varphi = \pi$).

The midplane gas density along the ring is given by $\rho(p,\varphi) = \Sigma_{\rm g}(p,\varphi)\Omega(r)/c_{\rm s}(r)$, where we have assumed for simplicity that $c_{\rm s}$ is independent of φ. According to equation (10), the azimuthal drag force acting per unit area of the dense particle disc is then given by

$$\begin{aligned} f_a(r,\varphi) = &-{\rm Re}_\star^{-1}\frac{GM_\star\Omega(r)}{rc_{\rm s}(r)} \\ &\times\Sigma_{\rm g}(p(r,\varphi),\varphi)\left[1-(1+e\cos\varphi)^{1/2}\right]^2. \end{aligned} \tag{D7}$$

We now compute the orbit-averaged azimuthal force acting on the particle ring by averaging $f_a(r, \varphi)$ over φ. To do this, we will assume that $\Sigma_g(p, 0) = \Sigma_{g,0}(p/p_0)^{-\theta}$, relate Σ_g to $\Sigma_g(p, 0)$ via equation (D4) and use expression (D2) to describe the dependence $p(r, \varphi)$. As a result, one finds that

$$\langle f_a(r)\rangle_\varphi = -\mathrm{Re}_\star^{-1}\frac{GM_\star\Omega(r)\Sigma_{g,0}}{rc_s(r)}\left(\frac{p_0}{r}\right)^\theta I(e,\theta), \tag{D8}$$

$$I(e,\theta) = \frac{(1+e)^{2+\theta}}{2\pi} \times \int_0^{2\pi}\frac{\left[1-(1+e\cos\varphi)^{1/2}\right]^2}{(1+e\cos\varphi)^\theta\left(1+2e\cos\varphi+e^2\right)}. \tag{D9}$$

We now explore the small-e limit of our results. When $e \to 0$, one can easily show that $I(e, \theta) \to e^2/8$ independent of θ, such that the orbit-averaged azimuthal force can be written as

$$\langle f_a(r)\rangle_\varphi = -\frac{e^2}{8\mathrm{Re}_\star}\frac{GM_\star\Omega(r)}{rc_s(r)}\Sigma_g(r). \tag{D10}$$

We use this result in Section 6.1 to demonstrate the enhancement of aerodynamic drag as the result of non-circular motions in the gaseous disc.

This paper has been typeset from a TEX/LATEX file prepared by the author.